Applied Catalysis B: Environment and Energy 385 (2026) 126274

Contents lists available at ScienceDirect

Applied Catalysis B: Environment and Energy

journal homepage: www.elsevier.com/locate/apcatb

# Catalytic ozonation of multi-component pharmaceutical mixtures: Kinetic evaluation, molecular interaction, including catalyst structure effects

Pasi Tolvanen [a,*], Ana Fernanda Núñez Núñez [a], Estéban Duverger [a], Nikke Saarinen [b], Abdul Shahid [a], Shey Jude Fale [a,g], Soudabeh Saeid [a,f], Matilda Kråkström [c], Narendra Kumar [a], Kari Eränen [a], Patrik C. Eklund [b], Jyri-Pekka Mikkola [a,d], Dmitry Yu. Murzin [a], Tapio Salmi [a,e]

[a] Laboratory of Industrial Chemistry and Reaction Engineering (TKR), Åbo Akademi University, Turku 20100, Finland
[b] Laboratory of Molecular Science and Engineering, Åbo Akademi University, Turku 20500, Finland
[c] Turku Bioscience Center, University of Turku and Åbo Akademi University, Turku 20520, Finland
[d] Technical Chemistry, Department of Chemistry, Chemical-Biological Centre, Umeå University, Umeå SE-901 87, Sweden
[e] Naples Industrial Chemistry Laboratory (NICL), University of Naples Federico II, Napoli 80126, Italy
[f] Linde + Robinson Laboratories, California Institute of Technology, Pasadena 91125, United States
[g] Novia University of Applied Sciences, Ekenäs, Finland

ARTICLE INFO

Dataset link: SEM images of Fe–H–Y and Fe–H–Beta zeolite catalysts (fresh and spent) used in catalytic ozonation of pharmaceutical mixtures

*Keywords:*
Catalytic ozonation
Advanced oxidation processes
Emerging contaminants
Pharmaceutical mixtures
Zeolites
Wastewater treatment
Transformation products
Reaction kinetics

ABSTRACT

Removal of pharmaceuticals from wastewater remains a major environmental challenge, requiring efficient and selective Advanced Oxidation Processes (AOPs). Catalytic and non-catalytic ozonation was investigated in a laboratory-scale reactor under optimized flow conditions (500–750 mL $min^{-1}$, 98 % $O_2$ feed). Ozonation kinetics of active pharmaceutical ingredient mixtures (APIs) consisting of ibuprofen (IBU), diclofenac (DCF), carbamazepine (CBZ), sulfadiazine (SDZ), and sulfamethoxazole (SFX) (40 mg $L^{-1}$ each) — was investigated using iron-modified zeolite catalysts, Fe-H-Y and Fe-H-Beta, under semi-batch operations (0.5 g catalyst, 20 °C) in order to correlate degradation and mineralization efficiency with catalyst structure, acidity, and stability. Both catalysts significantly improved the ozone utilization compared to non-catalytic ozonation. Interestingly, Fe-H-Y accelerated initial degradation rate, while the use of Fe-H-Beta resulted in the highest level of mineralization. Adsorption–desorption analysis revealed that the molecular size and polarity controlled the interactions between the pharmaceutical and the catalyst: smaller polar compounds (SDZ, SFX) exhibited stronger adsorption on the catalyst, while bulkier molecules (DCF, IBU) were restricted to external surfaces. Post-reaction characterization confirmed that the Fe-H-Y retained more surface area and exhibited lower Fe leaching, while Fe-H-Beta showed significantly higher carbon deposition. Overall, Fe-H-Y combined rapid kinetics and structural stability, while Fe-H-Beta provided higher mineralization, at the expense of more extensive fouling. The study demonstrated that optimized ozonation conditions, coupled with tailored zeolite catalysts, markedly improve the oxidation efficiency and long-term performance in the oxidation of pharmaceuticals.

## 1. Introduction

Pharmaceuticals are increasingly recognized as harmful contaminants of emerging concern in aquatic environment. Due to their continuous consumption and excretion, they are frequently detected in surface waters and municipal wastewater effluents at concentrations ranging from nanograms to several micrograms per liter. Commonly found substances include anti-inflammatories such as ibuprofen (IBU) and diclofenac (DCF), antibiotics like sulfadiazine (SDZ) and sulfamethoxazole (SFX), and antiepileptics such as carbamazepine (CBZ), see Fig. 1.

According to the studies conducted across Europe, concentrations of IBU in effluents typically range between 0.1 and 6 μg/L, while the DCF concentrations can exceed 1 μg/L [1–3]. Even at such low concentrations, several APIs have demonstrated adverse effects on aquatic organisms. Diclofenac, for instance, has been shown to damage fish kidneys and gills and affect osmoregulation and survival at sub-microgram levels [4–6] while ibuprofen disrupts the reproduction

* Corresponding author.
*E-mail address:* pasi.tolvanen@abo.fi (P. Tolvanen).

https://doi.org/10.1016/j.apcatb.2025.126274
Received 31 October 2025; Received in revised form 29 November 2025; Accepted 2 December 2025
Available online 3 December 2025

and growth in various invertebrates [7].

Conventional wastewater treatment plants are generally ineffective in removing this kind of micropollutants, as they are not designed to handle persistent and low-concentration organic compounds [8,9]. As a result, advanced oxidation processes (AOPs), particularly ozonation, have received growing attention due to their strong oxidation potential ($E^{\circ} = 2.076$ V vs the standard hydrogen electrode, SHE) and ability to degrade a wide range of organic compounds through both via direct electron transfer and indirect radical-based mechanisms [9]. However, the use of ozonation alone is associated with challenges such as incomplete mineralization, the need for high ozone doses, and the potential formation of harmful oxidation by-products [10,11].

As the global consumption of pharmaceuticals continues to rise, their release into aquatic environment is increasing, with potential risks for both the ecosystem and the human health and these risks are not yet fully understood. In recognition of these concerns, the revised Urban Wastewater Treatment Directive [12] of the European Union requires member states to implement quaternary treatment technologies, such as ozonation or use of activated carbon, to limit pharmaceutical emissions from wastewater treatment plants [12]. Recent studies in Nordic countries highlight the urgency of this effort. For example, Skalska-Tuomi *et al.* (2025) [13] reported concentrations of pharmaceutically active compounds in a Finnish municipal wastewater treatment plant reaching up to 263 μg $L^{-1}$ in the incoming wastewater, which were reduced to about 14 μg $L^{-1}$ in the treated water after conventional treatment, with further substantial removal achieved through quaternary treatment. These findings highlight both the persistence of APIs in treated wastewater, and the necessity of implementing advanced treatment processes in Europe.

To improve the performance of ozonation and reduce by-product formation, catalytic ozonation appears to be a promising route. By incorporating metal modified heterogeneous catalysts with varying structures, ozone decomposition can be promoted and additional reactive oxygen species can be generated, thereby enhancing degradation efficiency of the pharmaceuticals [14]. Among solid catalysts, metal-modified zeolites with different structures have received particular attention due to their stability, tuneable pore systems, and acidic surface functionalities [15].

### 1.1. Selection of catalysts

Zeolites were selected as catalyst supports because they offer well-defined, tuneable pore structures and acidity levels, enabling a systematic evaluation of how framework type and metal loading influence ozonation performance. Although diffusion limitations and moderate hydrothermal stability are recognized challenges for zeolites in aqueous media, they remain widely used benchmarks in catalytic ozonation due to their high chemical robustness, low metal leaching, and versatility in metal incorporation [15,16]. In this work, two iron-modified zeolites, Fe-H-Beta and Fe-H-Y, were chosen to represent distinct pore architectures and acidity profiles, allowing comparison between narrow-pore (Beta) and wide-pore (Y) frameworks. Full nomenclature and preparation details are provided in 2.2.

### 1.2. Insights from earlier work

Our group has systematically explored catalytic ozonation of selected pharmaceuticals (IBU, DCF, CBZ, and SDZ), with a particular attention to both parent compound removal and the fate of the transformation products (TP). A consistent outcome is that the choice of the catalyst strongly determines not only the kinetics of the parent degradation but also the accumulation or suppression of persistent by-products [6,17–22]

For ibuprofen (IBU), Saeid *et al.* demonstrated that metal-modified microporous zeolites with varying structures and acidities significantly enhance the degradation kinetics compared to non-catalytic ozonation. Among the tested catalytic materials, Cu-H-Beta-150-DP provided the highest removal rate, with almost complete conversion within 1 h, while also reducing the build-up of hydroxylated intermediates [17]. Fe- and Ni-modified catalysts improved the degradation kinetics, but copper was most effective by simultaneously accelerating the removal and suppression of persistent TPs. For carbamazepine (CBZ), non-catalytic ozonation produces large amounts of stable intermediates, mainly 1-(2-benzaldehyde)-4-hydro-(1 H,3 H)-quinazoline-2-one (BQM) and 1-(2-benzaldehyde)-(1 H,3 H)-quinazoline-2,4-dione BQD), which are both cytotoxic and persistent [18,21]. Screening of noble-metal catalysts revealed clear differences: Pt-H-Y-12 zeolite catalyst accelerated the BQM transformation, whereas Pd-H-Y-12 was the best in suppressing the accumulation of BQD, which remained $< 2$ mg/L after 2 h compared to $\approx 20$ mg/L in non-catalytic experiments. Copper-modified mesoporous catalysts promoted faster conversion of the intermediates BQM and BQD into downstream oxidation products, whereas Pd-modified Beta zeolites were less effective. For diclofenac (DCF), rapid degradation took place even without catalysts but chlorinated aromatic by-products such as 2,

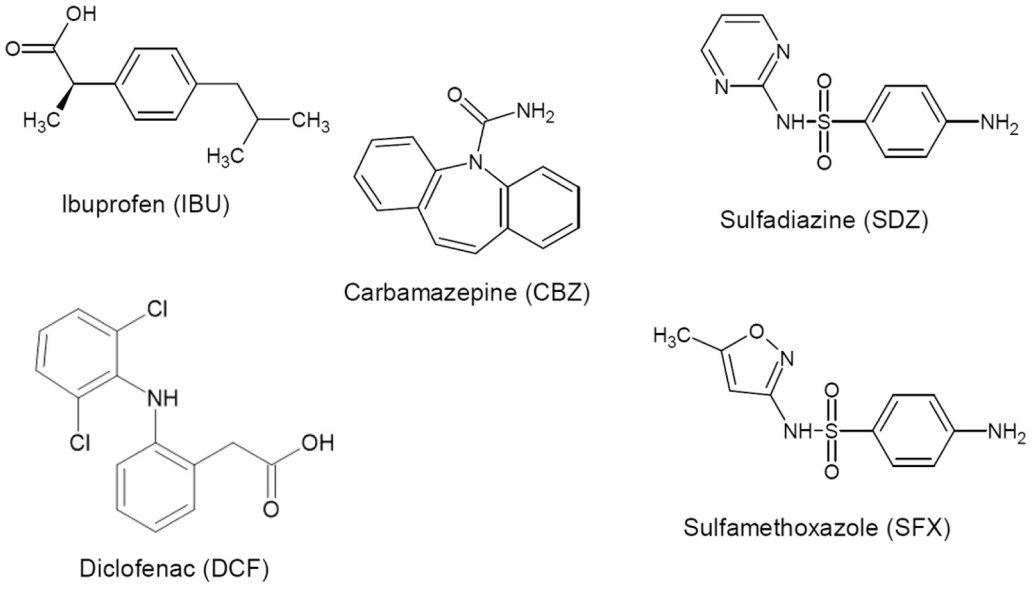


**Fig. 1.** Selected pharmaceuticals and their molecular structures.

6-dichloroaniline tended to persist [6]. The catalysts influenced this pathway differently: Pt-modified materials enhanced the DCF transformation and shifted the product spectrum towards more hydroxylated intermediates, whereas Pd- and Fe-based catalysts were less selective, sometimes retarding transformation. For sulfadiazine (SDZ), ozonation yielded a wide range of novel intermediates, most notably SDZ-P15, which accumulated up to 30 % of the starting concentration and was resistant to further breakdown [19]. Both Fe-H-Beta-25 and Cu-H-Beta-150 catalysts were studied, but rather than accelerating mineralization, they tended to slow down the SDZ conversion, highlighting that not all API classes benefit equally from the catalytic treatment.

In reality, APIs almost never occur as isolated contaminants; sewage effluents typically contain complex mixtures, with monitoring studies detecting 20–30 pharmaceuticals per site on average. Such mixtures pose risks beyond the sum of their parts, a phenomenon often referred to as the "cocktail effect." Even at individually sub-toxic concentrations, mixtures of pharmaceuticals can induce oxidative stress and enzymatic disruption in aquatic organisms and lead to changes in the types and abundance of microbial, algal, and invertebrate species [7,23,24].

### 1.3. Aim and scope of this work

This study investigates the catalytic ozonation of five widely detected pharmaceuticals—ibuprofen (IBU), diclofenac (DCF), carbamazepine (CBZ), sulfadiazine (SDZ), and sulfamethoxazole (SFX) — examined both individually and in mixtures. The aim is to elucidate how catalyst structure and molecular properties of the target compounds influence degradation kinetics, competitive effects, and transformation pathways under both catalytic and non-catalytic conditions. The results contribute to developing efficient, selective, and scalable advanced oxidation processes for wastewater treatment.

## 2. Materials and methods

### 2.1. Chemicals and reagents

Ibuprofen sodium salt (IBU, ≥98 %) and diclofenac sodium salt (DCF, ≥98 %) were obtained from Sigma-Aldrich (USA), while carbamazepine (CBZ, ≥99 %), sulfadiazine (SDZ, ≥98 %), and sulfamethoxazole (SFX, ≥98 %) were purchased from Alfa Aesar (UK). The sodium salt forms of IBU and DCF were used due to their significantly higher solubility in water, enabling accurate preparation of stock solutions and reproducible initial concentrations. HPLC-grade solvent acetonitrile was used in chromatographic analyses. Potassium iodide (Sigma-Aldrich), 0.1 molar sodium thiosulfate (Merck) were used for ozone quantification. Aqueous solutions were prepared with ultrapure Milli-Q water which had resistivity ≥ 18.2 MΩ·cm.

### 2.2. Catalyst synthesis and characterization

The Fe-modified zeolites used in this work represent two framework types: Beta (BEA) and Y (FAU). Zeolite Beta (Fe-H-Beta-25-EIM) contains three-dimensional 12-membered-ring channels (~0.67–0.76 nm), whereas Zeolite Y (Fe-H-Y-30-EIM) consists of large supercages (~1.3 nm) interconnected by 12-membered-ring windows (~0.74 nm), as illustrated in Fig. 2.

For clarity, the full synthesis notation is provided here but simplified elsewhere. Fe-H-Beta-25-EIM refers to Fe-impregnated H-Beta with SiAl = 25, and Fe-H-Y-30-EIM to Fe-impregnated H-Y with SiAl = 30, both prepared by the evaporation–impregnation (EIM) method. Throughout the manuscript, these materials are denoted simply as Fe-H-Beta and Fe-H-Y.The catalysts were synthesized by evaporation–impregnation using ferric nitrate as the iron precursor. The iron solution was mixed with the parent zeolite (Zeolyst International) and rotated for 24 h at 60 °C. After solvent removal, the solid was dried at 100 °C and calcined at 450 °C for 3 h. The final samples were sieved to 125–250 μm and stored in a dry environment.

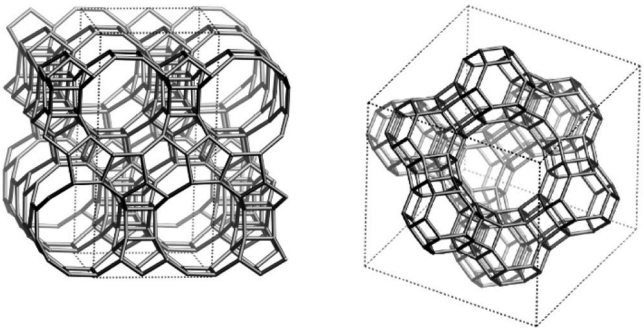

**Fig. 2.** Framework topologies of zeolites: left: BEA (Beta), showing the 3D network of 12-membered rings (pore diameters 0.55 × 0.55 nm and 0.76 × 0.64 nm); right: FAU (Y), showing supercages (~1.3 nm) connected by 12-membered-ring windows (~0.74 nm). Adapted from IZA.") [25].

Physicochemical characterization included $N_2$ physisorption (Micromeritics 3FLEX) for surface area and pore analysis, X-ray diffraction (XRD) for crystallinity, scanning electron microscopy coupled with energy-dispersive X-ray spectroscopy (SEM–EDX, Zeiss Leo Gemini 1530) for morphology and composition, FTIR with pyridine adsorption for acidity, transmission electron microscopy (TEM) for crystal morphology, and thermogravimetric analysis (TGA) for thermal stability and organic deposition.

### 2.3. Ozonation setup and experimental design

Ozone was produced in-situ with the aid of an ozone generator (Absolute Ozone, Nano model, Canada), fed with synthetic gas mixtures (oxygen/nitrogen) and introduced into the liquid phase through a sintered glass frit which was placed inside a 250 mL glass reactor. The temperature was maintained at 20 ± 0.5 °C using a water bath and recorded to a computer for the duration of the entire experiment. The gas flow was controlled with mass flow controllers for each gas ($O_2$/$N_2$). The experiments were carried out in a SpinChem® rotating bed reactor (RBR) fitted inside a flower-baffled glass vessel [26]. The RBR design provides efficient mixing and high turbulence while confining the catalyst particles within a rotating basket, thereby functioning simultaneously as a mechanical stirrer and as a containment system for the solid catalyst [27]. Since the RBR has a hole at the bottom centre, a high enough rotation rate creates a powerful flow of the liquid through the compartments where the catalyst particles are immobilized, ensuring an efficient mass transfer of the dissolved ozone to the catalyst surface and inside of the pores, i.e. minimizing mass transfer limitations which may occur in a typical slurry reactor. The reactor setup and the rotating bed reactor unit are illustrated in Fig. 3.

### 2.4. Ozone mass transfer, control and stability experiments

KI-based titration studies were conducted by two different methods to optimize the flowrates and stirring speeds for the best possible ozone mass transfer. In the first approach the reactor was filled with a 1 L solution of 0.1 M potassium iodide (KI) prepared in deionized water. Various gas compositions ($O_2$: 90–98 v-%), gas flowrates (125–500 mL $min^{-1}$) and stirring speeds (250–1000 rpm) were screened to optimize the ozone production as well as the ozone mass transfer into the liquid phase. Iodometric titration was performed to determine the ozone concentration in the liquid phase. The principle of this iodometric titration is that dissolved ozone oxidizes iodide ions ($I^-$) to iodine ($I_2$) according to eq. 1

$$O_3 + 2I^- + H_2O \rightarrow O_2 + I_2 + 2OH^- \quad (1)$$

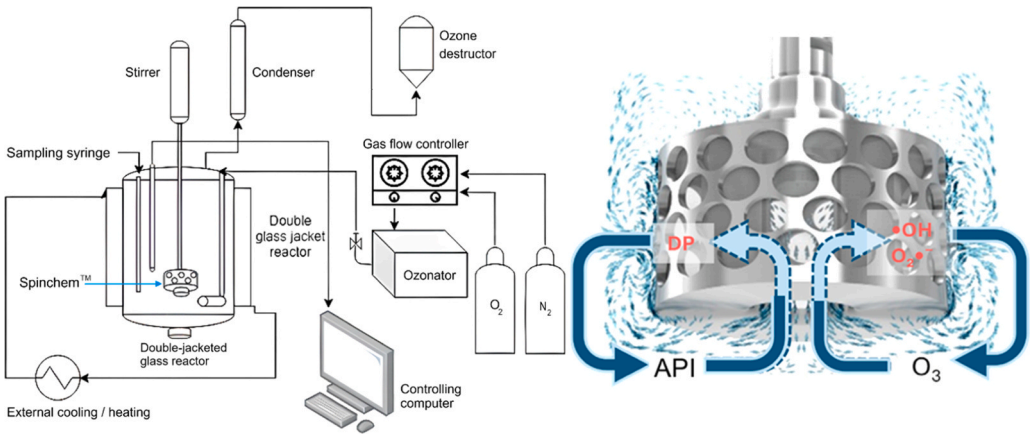


**Fig. 3.** The ozonation reactor setup, and the Spichem® rotating bed reactor used for holding the catalyst particles as well as for enhancement of the mass transfer between the three phases.

and the formed $I_2$ is subsequently titrated with a standardized sodium thiosulfate solution, allowing the ozone concentration to be quantified from stoichiometry.

In a second type of experiment, the behaviour of ozone was examined in the presence of the solid catalyst. In this case, the reactor water was first pre-ozonated to saturation, after which ozone feeding was stopped, and the catalyst powder (here: 0.30 g) was added. The decay of dissolved ozone was then followed by periodic KI titration of withdrawn samples.

In addition, preliminary stability tests were conducted for the pharmaceutical stock solutions to verify that no degradation occurred during storage prior to ozonation. The tests were performed at room temperature and at 60 °C, and the results are presented in Supplementary material S7.

Several control experiments were conducted, such as using pure $O_2$ with $N_2$ instead of ozone (i.e. the ozonator was simply not turned on, otherwise an identical experiment); or using no catalyst (non-catalytic ozonation); as well as switching off the gas flow, in order to investigate how the different APIs may adsorb from the liquid phase into the surface or diffuse in the pores of the solid catalyst particles (adsorption/desorption study). The reactor was exposed to ambient laboratory light (no UV source), which may cause minor photolytic degradation of for instance, Diclofenac as reported by Li *et al.* [28]. Additionally, experiments were conducted to investigate how the presence of solid catalyst influences the decomposition of dissolved ozone in the liquid phase.

### 2.5. Experimental matrix

Ozonation experiments were performed in several series: first, each individual API (40 mg/L) was ozonated in the absence of catalysts, followed by non-catalytic ozonation of binary mixtures (2 APIs at 40 mg/L each). Finally, non-catalytic ozonation was carried out with a full mixture of five APIs mixed together (each with 40 mg/L). Throughout the manuscript, this system is referred to as the five-component mixture (or 5-API mixture in figures and tables. Similarly, catalytic ozonation experiments were conducted with single, binary and five API mixtures and using identical reaction conditions for comparison. The temperature was always 20°C and it was controlled by external heating-cooling device. Two different iron-based catalysts were used, Fe-H-Beta and Fe-H, which were both synthesised using the evaporation impregnation method. Each experiment was performed once, except the non-catalytic ozonation of IBU, to evaluate the reproducibility. The experiments are summarized in SI Table S1.

### 2.6. Ozonation procedure

Prior to each experiment, the ozone generator (Absolute Ozone® Nano) was stabilized for at least 20 min to reach a steady-state conversion of oxygen to ozone. This warm-up period is necessary because the corona discharge efficiency and gas temperature require equilibrium before the output concentration of ozone becomes constant. The ozonation reactor was operated in a semi-batch mode. Before introducing the pharmaceutical mixture, the aqueous phase was first saturated with ozone under the selected gas-flow conditions. Ozone was continuously bubbled through 1 L of deionized water until the concentration of dissolved ozone reached a steady plateau, corresponding to gas–liquid mass-transfer equilibrium. The duration of this pre-saturation step depended on the gas flow rate (typically 20 min), as is later illustrated in the section on ozone-transfer dynamics (Fig. 7). Once the aqueous phase was saturated, a defined volume of the pharmaceutical stock solution was injected into the reactor to initiate the degradation reaction (t = 0 min). This procedure ensured a reproducible initial ozone concentration in the liquid and avoided the transient build-up phase that occurs if ozone generation and solubilization start simultaneously with the reaction. When a heterogeneous catalyst was used, it was placed inside the SpinChem® rotating bed compartments before the start of the water-saturation step, ensuring that gas–liquid–solid contact was established already during ozone dissolution. The catalyst mass in the kinetic experiments was always 0.50 g, except in the adsorption–desorption and non-API ozonation studies, where 0.30 g was used to reduce catalyst consumption in non-critical tests.

### 2.7. Analytical methods

HPLC-DAD (Agilent 1260 Infinity) was used to quantify the API concentrations, employing a C18 reverse-phase column. Mobile phases included water/acetonitrile with the isocratic flow ratio of 30/70. The flow of eluent was 0.4 mL $min^{-1}$ , ensuring that no overlapping peaks appeared between the initial reactants. With a higher flow rate, especially the APIs sulfadiazine and sulfamethoxazole overlap partially. The investigated APIs were detected accurately at the used wavelength of 222 nm. Calibration curves were established from standard solutions (1–100 mg/L), with $R^2 > 0.998$. The studied APIs were with the above mentioned parameters eluted in the time window 6.74 min (SDZ) – 15.76 min (IBU). A complete table of retention times and corresponding statistics is provided in SI Table S2. For investigation of short-chain organic acids, selected samples were examined using a SUPLECOGEL C-610H column (30 cm × 7.8 mm I.D., 9 μm). The mobile phase consisted of 0.05 % $H_2SO_4$ in water, with a flow rate of 0.4 mL $min^{-1}$ and a column temperature of 30 °C. Detection was carried out at 210 nm (UV).

The SUPLECOGEL C-610H column is a cation-exchange column packed with sulfonated polystyrene–divinylbenzene in hydrogen form ($H^+$), designed for separation of small organic acids, alcohols, and other polar molecules in aqueous systems.

The pharmaceuticals and their transformation products were analyzed using LC–MS. An Agilent 6460 triple quadrupole mass spectrometer equipped with an electrospray ionization (ESI) source was employed in multiple reaction monitoring (MRM) mode for sensitive quantification. Chromatographic separation was carried out on a Waters Acquity UPLC BEH C18 column (2.1 × 100 mm, 1.7 μm), with a water-acetonitrile gradient (0.4 mL $min^{-1}$, injection volume 1 μL). The retention times were determined individually for each API, and calibration curves were established to allow the quantification. LC–MS was further used to identify the transformation products during ozonation, providing structural insights into the intermediates formed.

Transformation products (TPs) formed during ozonation and catalytic ozonation were analyzed using an Agilent 6460 triple quadrupole LC–MS/MS system operated in multiple-reaction-monitoring (MRM) mode. Structural assignment was performed using a previously developed MRM method optimized in earlier single-API studies [6,17–22]. The method was originally established and validated using authentic standards or tentatively identified transformation products, and the present analysis compared retention times and transition ratios to those reference data. A retention time shift of ±0.10 min relative to the established library was accepted. Identification confidence followed the Schymanski scale (Levels 2a–3). A complete list of detected TPs and their confidence levels is provided in Supplementary material Table S6. All molecular structures of APIs and transformation products identified or referenced in this work are provided as MOL files in the Supplementary Information Table S7.

The extent of mineralization was assessed via total organic carbon (TOC) analysis. TOC was determined by catalytic combustion at 680 °C (Shimadzu TOC-V CSN) using subtraction of inorganic carbon (IC) from total carbon (TC).

## 3. Results and discussion

### 3.1. Catalyst structure and surface properties

#### 3.1.1. Scanning electron microscopy coupled with energy dispersive X-rays microscopy

Scanning electron microscopy (SEM) combined with energy-dispersive X-ray spectroscopy (EDX) revealed the surface morphology and elemental composition of the Fe-modified zeolite catalysts. SEM images (Fig. 4a-d) confirmed distinct topographical features characteristic of the two zeolite frameworks: Fe-H-Beta exhibited irregular, nanosized crystallites with slight agglomeration, whereas Fe-H-Y displayed the well-known triangular crystals typical for Y-zeolites. Despite minor particle aggregation, both materials preserved a homogeneous microcrystalline texture.

Elemental analysis by EDX verified the presence of Fe predominantly as surface iron oxide ($Fe_2O_3$), consistent with the synthesis route that excluded a reduction step. Quantitatively, the Fe-H-Beta contained ~20.2 wt% $Fe_2O_3$, compared to ~15.5 wt% for Fe-H-Y, indicating slightly higher iron loading on the Beta framework. Both catalysts also showed expected proportions of $SiO_2$ and $Al_2O_3$, confirming retention of the zeolitic matrix.

Importantly, SEM/EDX performed on spent catalysts, after two hours of ozonation of the five-component mixture, (Fig. 4c-d) revealed no significant morphological degradation or leaching of iron. Table 1 shows that the $Fe_2O_3$ content remained essentially constant (18.5 % for Beta, 15.5 % for Y), suggesting robust catalyst stability under the actual

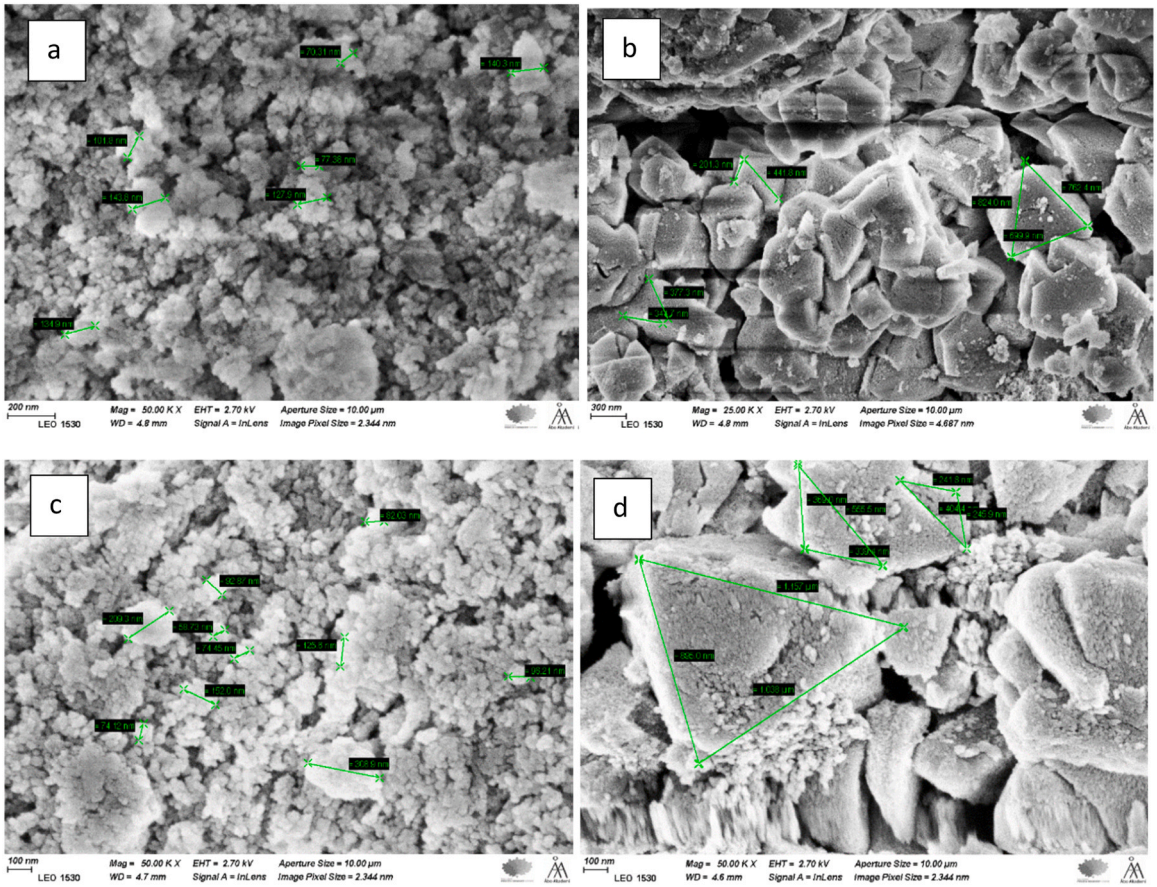


**Fig. 4.** SEM images for a) fresh Fe-H-Beta and b) fresh Fe-H-Y, c) spent Fe-H-Beta, d) spent Fe-H-Y. 50k magnification.

**Table 1**
Elemental composition on the fresh and spent (five-component mixture) catalyst surfaces, expressed in weight-%.

| | Catalyst | $Al_2O_3$ | $SiO_2$ | $Fe_2O_3$ |
|---|---|---|---|---|
| Fresh | Fe-H-Beta | 5.3 | 73.9 | 20.2 |
| | Fe-H-Y | 4.8 | 79.6 | 15.5 |
| Spent | Fe-H-Beta | 4.1 | 77.4 | 18.5 |
| | Fe-H-Y | 2.7 | 81.9 | 15.5 |

ozonation conditions. The slight decrease in $Fe_2O_3$ for Beta from 20.2 to 18.5 wt-.% suggests minor leaching, yet the framework remained intact and the majority of iron was preserved, indicating good and acceptable stability under ozonation conditions. These findings support earlier observations that the Fe-oxide species at the surface of H-Beta and H-Y zeolite catalysts provide active sites for the ozone activation, while the zeolitic framework ensures mechanical integrity during reaction cycles.

### 3.1.2. FTIR and acidity (pyridine-FTIR)

Framework FTIR confirmed the characteristic zeolitic T–O–T vibrations for both Fe-H-Beta and Fe-H-Y, indicating that the Fe impregnation preserved the parent structures. Acid sites were quantified by pyridine-FTIR, which showed the diagnostic bands at ≈ 1540 $cm^{-1}$ for Brønsted (BAS) and ≈ 1450 $cm^{-1}$ for Lewis (LAS) acid sites. For the fresh catalysts, Fe-H-Beta displayed a higher density of the Lewis sites (263 μmol $g^{-1}$ vs. 155 μmol $g^{-1}$ for Fe-H-Y), while the Brønsted acidity was comparable for the two materials (120 vs. 94 μmol $g^{-1}$).

After ozonation of the five-component mixture (2 h), Fe-H-Beta showed a moderate loss of acidity (BAS −22 %; LAS −27 %), consistent with partial site masking by retained organics. In contrast, Fe-H-Y exhibited only a slight decrease in Lewis acidity (−7 %) and a modest increase in Brønsted acidity (+15 %). This apparent gain likely reflects unmasking of previously inaccessible OH groups or changes in pyridine adsorption equilibria within the wider Y-zeolite pores, rather than formation of new sites. These trends are consistent with TGA and adsorption–desorption data, which indicate higher accumulation of organic residues in Beta. Unlike earlier studies [17,21] reporting only fresh catalyst acidity, our results demonstrate that spent-catalyst measurements can reveal changes in site accessibility under realistic ozonation conditions [17,21].

After regeneration, Fe-H-Beta recovered part of its Brønsted acidity (+14 % BAS), while its Lewis acidity changed only slightly (−5 % vs. spent). Fe-H-Y showed a reduction in both BAS (−19 %) and LAS (−24 % vs. spent), indicating framework-dependent differences in how the acid sites respond to thermal treatment. Overall, the coexistence of surface $Fe_2O_3$ species with preserved Brønsted and Lewis acidities highlights the dual function of these materials: Fe provides redox-active sites for ozone activation, while the zeolite framework contributes to acid functionalities that can stabilize intermediates. Thus, Beta is more susceptible to pore blockage by organic species, while Y retains the accessibility under ozonation but can lose sites upon regeneration.

Pyridine-FTIR was evaluated at 150, 250, and 350 °C to assess the distribution of weak, medium, and strong acid sites, respectively. Fig. 5 below presents the total accessible acidity at 150°C, while the higher-temperature results are provided in the Supplementary material S5. The results confirm that both catalysts retained medium and strong acid sites, where Fe-H-Y had a relatively higher fraction of thermally stable LAS compared to Fe-H-Beta.

The acidity results further support the observed catalytic behaviour. Fe-H-Beta exhibited a more pronounced loss of Brønsted sites after ozonation (-27 %), which is consistent with stronger adsorption of polar

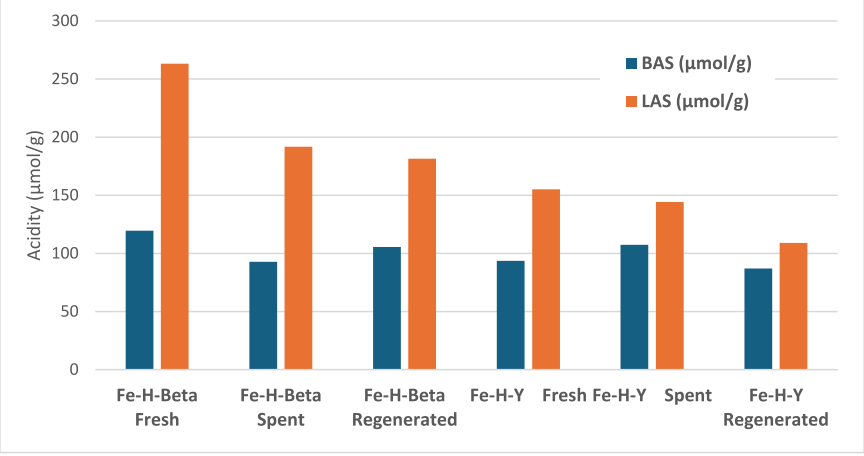


**Fig. 5.** Acidity measurements of fresh, spent and regenerated beta and Y-zeolites at 150°C.

**Table 2**
Nitrogen adsorption of fresh, spent, and regenerated catalysts used.

| Catalyst | Condition | $S_{BET}$ ($m^2/g$) | $S_{D-R}$ ($m^2/g$) | $V_t$ ($cm^3/g$) | $V_\mu$ ($cm^3/g$) | d (nm) |
|---|---|---|---|---|---|---|
| Fe-H-Beta | Fresh | 561 | 673 | 0.565 | 0.184 | 0.672 |
| Fe-H-Beta | Spent (five-APIs) | 417 | 529 | 0.377 | 0.092 | 0.705 |
| Fe-H-Beta | Regenerated | 402 | 513 | 0.368 | 0.098 | 0.730 |
| Fe-H-Y | Fresh | 585 | 788 | 0.353 | 0.226 | 0.755 |
| Fe-H-Y | Spent (five-APIs) | 577 | 770 | 0.348 | 0.185 | 0.761 |
| Fe-H-Y | Regenerated | 580 | 775 | 0.350 | 0.179 | 0.758 |

$S_{BET}$ = BET surface area;
D-R = Dubinin–Radushkevich method;
$V_\mu$ = micropore volume;
$V_t$ = total pore volume;
d = average pore diameter (calculated as $4 \times V_t / S_{BET}$).

by-products and persistent pore blockage. In contrast, Fe-H-Y retained and slightly increased its Brønsted acidity (+15 %), reflecting its greater structural robustness and its ability to maintain accessible active sites. This correlation between the acidity retention and catalytic activity confirms that both pore architecture and acid site stability influence the long-term performance in multi-component ozonation.

### 3.1.3. Nitrogen physisorption

The textural properties of the Fe-modified zeolites were analyzed by nitrogen physisorption. The results are collected in Table 2. Both Fe-H-Beta and Fe-H-Y exhibited type IV isotherms with H4 hysteresis, characteristic for mesoporous materials containing significant microporosity.

For the fresh catalysts, the B.E.T. surface areas were 561 and 585 $m^2$ $g^{-1}$ for Fe-H-Beta and Fe-H-Y, respectively, with total pore volumes of 0.56 and 0.35 $cm^3$ $g^{-1}$ . Beta had a larger total pore volume but a narrower median pore width (0.67 nm), while Y possessed a slightly larger pore size (0.75 nm) and a higher micropore fraction (0.23 vs. 0.18 $cm^3$ $g^{-1}$). Surface area of the catalysts were measured using the Dubinin method and micropore volume by Dubinin–Radushkevich (D–R).

After ozonation of the five-component mixture, both catalysts displayed textural changes, but to very different extents. Fe-H-Beta suffered pronounced losses: the specific surface area decreased by ~26 %, total pore volume by ~33 %, and micropore volume by ~50 %. This strong decline indicates significant pore blockage by retained organics, being consistent with TGA and FTIR acidity results. Regeneration only partially restored the textural properties (micropore volume remained ≈ 0.1 $cm^3$ $g^{-1}$), suggesting that the deposits were not fully removed. Notably, this contrasts with earlier findings on single-API ozonation of ibuprofen, where regeneration of Fe-H-Beta largely restored the surface area and micropore fraction [17]. The weaker recovery observed here probably reflects the more complex composition of the multi-component pharmaceutical mixture, which generates a broader variety of persistent and strongly adsorbed residues that are more difficult to eliminate by calcination.

In contrast, Fe-H-Y maintained its structural integrity with only marginal changes: the total pore volume decreased only by 1–2 %, and micropore volume by ~18 %. The external surface area and porosity were largely preserved, and regeneration gave values close to those of the fresh catalyst. This highlights the superior robustness of the Y-zeolite framework compared to Beta.

Overall, the results show that the textural stability of the catalysts is strongly framework-dependent. The narrower pores of Fe-H-Beta make it more susceptible to blockage and surface-area loss during multi-component ozonation, whereas the wider and more open structure of Fe-H-Y maintains pore accessibility and stability, supporting more sustained catalytic performance.

### 3.1.4. Transmission electron microscopy

Transmission electron microscopy (TEM) analysis of the Fe-H-Beta catalyst (Fig. 6) revealed well-defined crystalline particles with typical dimensions of 300–500 nm and the faceted morphology characteristic of Beta-type zeolites. The imaging confirmed a uniform particle size distribution and preserved framework integrity, with no observable structural degradation, agglomeration, or pore collapse. TEM is particularly valuable for assessing fine structural features and the dispersion of metal species, and the micrographs here indicate that the Fe impregnation and post-treatment steps did not alter the crystal morphology.

### 3.1.5. Thermogravimetric analysis (TGA)

In the five-component API catalytic ozonation experiments 0.5 g of catalyst was used with a total of 200 mg of APIs (five compounds at 40 mg $L^{-1}$ each). Thermogravimetric analysis was used to evaluate the thermal stability of the catalysts and to estimate the extent of organic deposition after ozonation of the five-component mixture.

The total weight loss up to 800 °C was 8.9 % → 14.2 % for Fe-H-Beta (fresh → spent) and 10.8 % → 14.5 % for Fe-H-Y, confirming overall thermal stability for both materials. To quantify organic deposits, the low-temperature weight loss (≤ 250 °C) was evaluated and the increase relative to the fresh baseline was used as an indicator of retained carbonaceous material. For Fe-H-Beta, this loss increased from 24.8 to 47.9 mg $g^{-1}$ , corresponding to an incremental load of 23.0 mg $g^{-1}$ (≈ 2.3 wt%); for Fe-H-Y, it increased from 29.4 to 37.1 mg $g^{-1}$ (≈ 0.77 wt %). These increments correspond to approximately 11.5 mg and 3.9 mg of retained carbonaceous matter per 0.5 g of Fe-H-Beta and Fe-H-Y, respectively—equivalent to about 5.8 % and 1.9 % of the total initial

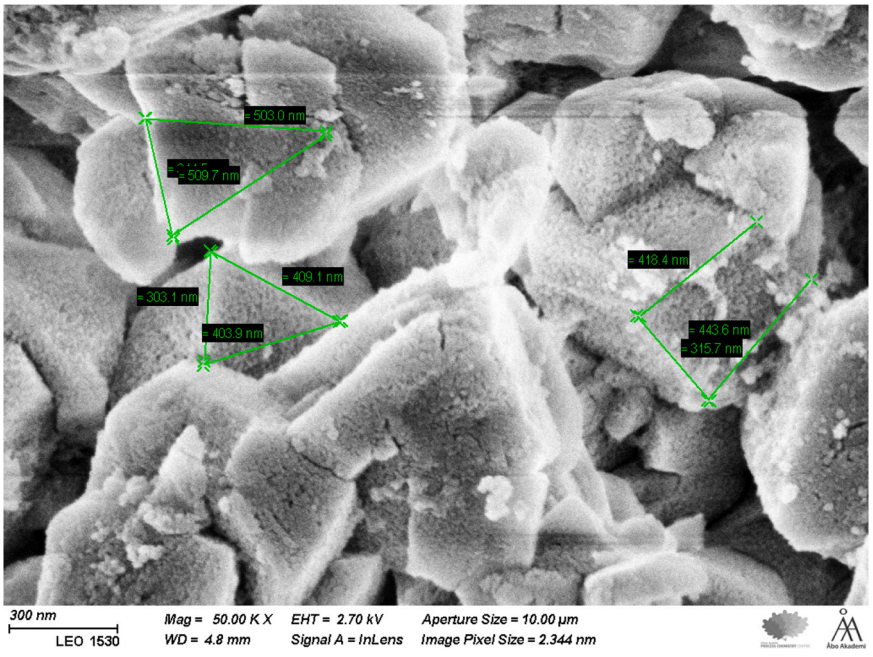


**Fig. 6.** TEM micrograph of Fe-H-Beta catalyst showing well-formed Beta crystals (300–500 nm) with preserved morphology and no signs of structural degradation after Fe impregnation.

organic load (200 mg APIs). The higher retained carbon fraction for Fe-H-Beta indicates stronger adsorption and trapping of partially oxidized by-products within its narrower micropore network and on its more acidic external surface.

In summary, both catalysts retained excellent thermal stability, with no structural decomposition detected up to 800 °C, indicating that the observed mass losses are primarily due to desorption or oxidation of residual organic species rather than the framework degradation.

### 3.1.6. Structure–activity relationships

The characterization results collectively show that the catalytic behaviour of Fe-H-Beta and Fe-H-Y is governed by their acidity, pore topology and stability. Fe-H-Y maintains higher Brønsted acidity and structural integrity after reaction, which correlates with its faster initial kinetics and lower Fe leaching. In contrast, the narrower pore system and higher external surface contribution of Fe-H-Beta favour deeper oxidation and increase mineralization, but also lead to more carbon deposition as observed in TGA and SEM analyses. The larger supercages of the Y-framework facilitate access for bulkier APIs, whereas the Beta framework imposes stronger steric constraints, consistent with the adsorption trends. Overall, the combined structural features explain why Fe-H-Y exhibits superior stability and rapid initial degradation, while Fe-H-Beta promotes more extensive mineralization.

## 3.2. Kinetic ozonation experiments

### 3.2.1. Analytical method validation, API stability, and ozone mass transfer control

During ozonation, the APIs formed a variety of more polar transformation products—such as hydroxylated, nitrated, and ring-opened derivatives—resulting in several additional peaks between 4 and 6 min, generally distinct from the parent compounds. An example of an HPLC chromatogram for the non-catalytic ozonation of the five-API mixture is shown in Fig. 7a. The chromatograms reveal that new, early eluting products appear predominantly between 4 and 6 min, with the most intense peak observed at 5.47 min after 5 min (red line) and 30 min (green line) of reaction. These products are likely moderately polar oxidation intermediates rather than the very short-chain carboxylic acids, which typically show little retention and weak UV response under the applied reversed-phase conditions. The consistent appearance of the 5.47 min peak across multiple degradation profiles nevertheless suggests the formation of a relatively stable intermediates that warrants

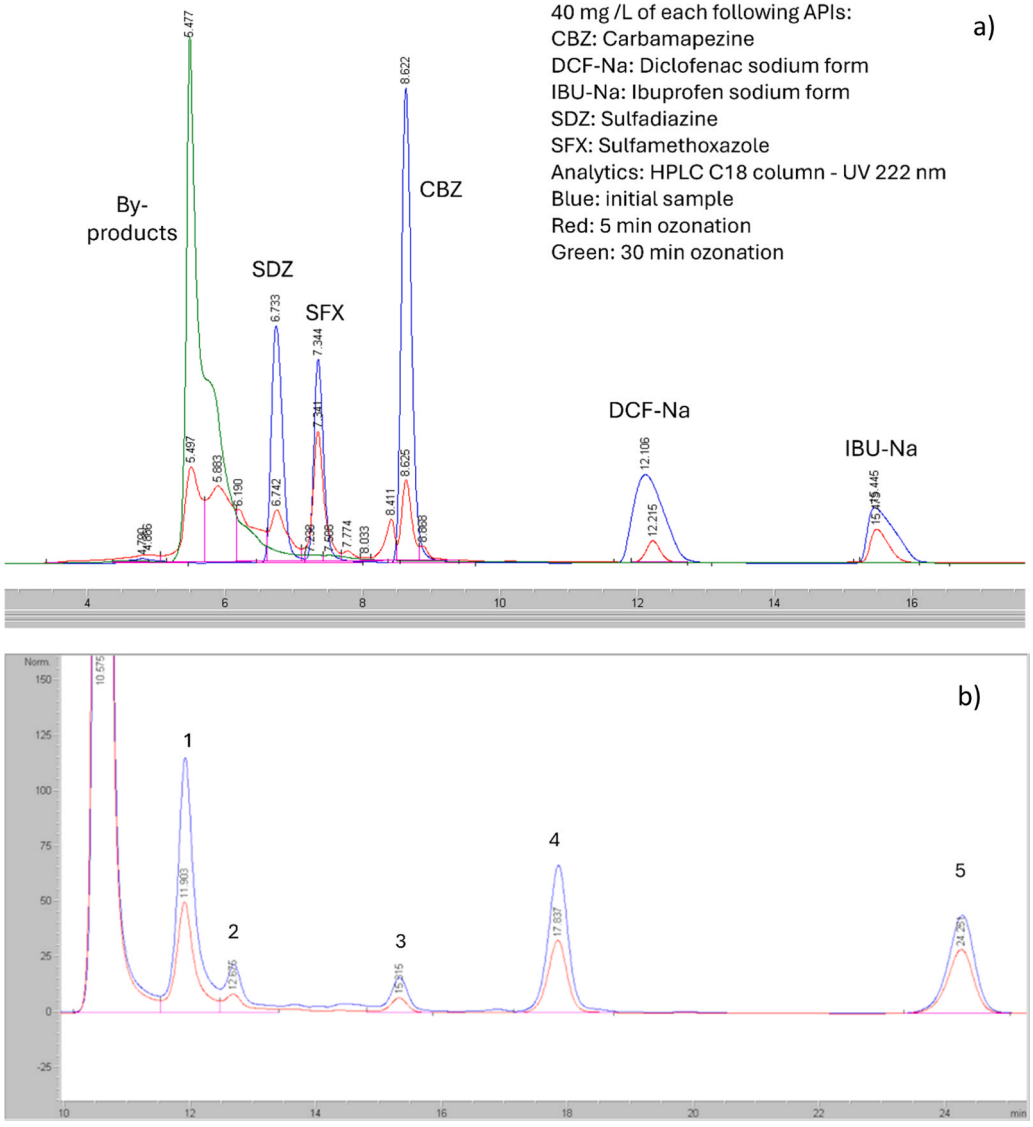


**Fig. 7. a)** Chromatographic responses of simultaneous non-catalytic ozonation of all five APIs. and **b)** Identification of low molecular weight carboxylic acids from catalytic five-component final samples (blue = Fe-H-Y; red = Fe-H-Beta catalysts). 1–5 corresponds to detected (but not identified) acids, whereas peak at t = 10 min is not an acid but a coeluting compound from the eluent.

further structural methods. In Fig. 7b, the similar samples were analysed with a column that is more suitable for identification of short-chain carboxylic acids (SUPLECOGEL C-610H (30 cm × 7.8 mm ID, 9 μm. From this analysis, some short-chain carboxylic acids were detected, confirming partial mineralization of intermediates. Their overall abundance was lower for the Fe–H–Beta catalyst compared to Fe–H–Y, consistent with its somewhat higher TOC removal efficiency, which will be discussed in Section 3.6.2.

Prior to kinetic experiments, stability tests were carried out to ensure that the pharmaceutical mixtures did not degrade in the absence of ozone and/or catalyst. Binary mixtures and the five-component mixture were kept under constant stirring in 10 mL vials both at room temperature and inside an oven at 60°C. Weekly HPLC monitoring during one month confirmed that the compounds remained stable over prolonged timescale, showing neither significant concentration decrease nor formation of transformation products. These results established that any observed degradation in later experiments was solely attributable to the ozonation process. The stability test results are provided in Supplementary material S7.

The initial plan included metoprolol as one of the APIs. However, metoprolol displayed signs of instability and unpredictable behaviour under the HPLC analysis of binary mixtures, making it an unsuitable candidate for reliable kinetic evaluation. For this reason, it was replaced by sulfamethoxazole (SFX) in the final experimental matrix (Fig. 1). While no separate stability tests were repeated for the SFX-containing mixtures, its inclusion is based on several literature studies reporting its stability in aqueous solutions in the absence of oxidants [29,30], as well as our own blank test in ozonation experiments where no spontaneous decay was detected in samples.

The effect of gas flow rate on ozone dissolution was examined to determine the mass-transfer coefficient ($k_La$) under the experimental conditions. As shown in Fig. 8, both the equilibrium dissolved ozone concentration and the rate of saturation increased with flow rate. The highest flow (750 mL $min^{-1}$) achieved a steady-state concentration of about 45 mg $L^{-1}$ with $k_La = 0.199$ $min^{-1}$ , whereas lower flows (150 and 250 mL $min^{-1}$) reached 16 and 32 mg $L^{-1}$ with $k_La = 0.084$ and 0.155 $min^{-1}$ , respectively. The excellent fit between the experimental data and the model confirms that the system is well-described by first-order mass-transfer kinetics and that ozone transfer can be optimized effectively by adjusting the gas feed rate. Symbols represent measured data, and solid lines correspond to the model fits using the mass-transfer expression

$$C_t = C^*(1 - e^{-k_L a \bullet t}) \quad (2)$$

where C* is the equilibrium concentration and $k_La$ the overall mass-transfer coefficient. The fitted $k_La$ values were 0.084, 0.155, and 0.199 $min^{-1}$ for the 150, 250, and 750 mL $min^{-1}$ flow rates, respectively. The results show that increasing gas flow enhances both ozone saturation (from ≈16–45 mg $L^{-1}$) and mass-transfer rate, confirming that the optimized high-flow condition maintains near-saturated ozone levels during catalytic ozonation experiments. Though the theoretical equilibrium solubility of ozone in water is independent of flow rate, the apparent steady-state concentrations measured here (16–45 mg $L^{-1}$) reflect a dynamic balance between gas–liquid transfer and ozone decomposition. At higher gas flows, faster mass transfer and shorter residence time in the reactor minimize ozone losses, allowing the system to approach the near-saturation limit.

Because the gas stream exiting the ozonator still consisted predominantly of oxygen, several control experiments were carried out to confirm that the observed pharmaceutical degradation arose from ozone-driven and catalytic reactions rather than from experimental artefacts or the effect of oxygen itself.

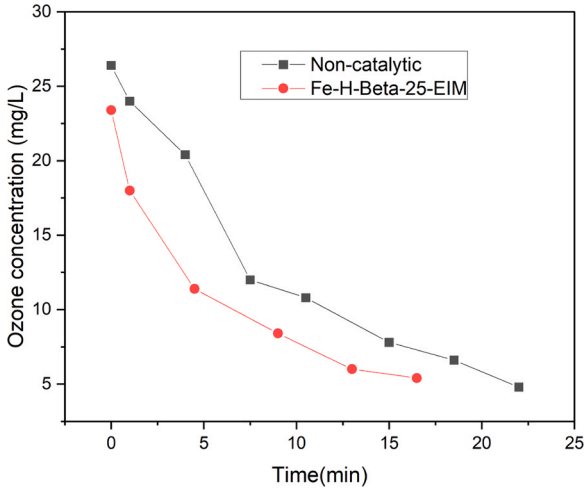


**Fig. 9.** Ozone decay in the absence of pharmaceuticals in the presence or absence of catalyst.

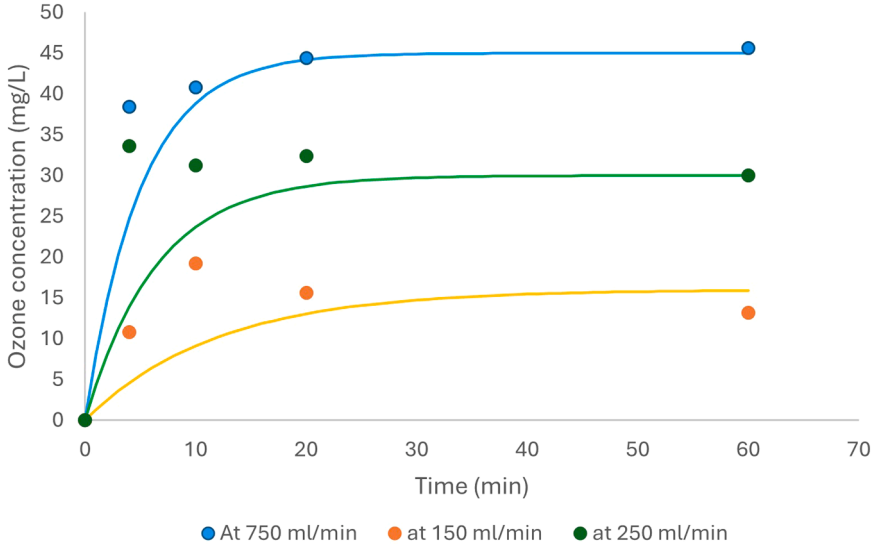


**Fig. 8.** Experimental and modelled dissolved ozone concentrations as a function of ozonation time for different gas flow rates (150, 250 and 750 mL $min^{-1}$) in pure water at 20 °C.

The stability of ozone in water was evaluated in the absence of pharmaceuticals. The results are displayed in Fig. 9. After a prolonged saturation period (20 min for saturation), the gas feed was stopped, and the dissolved ozone concentration was monitored over time in the absence and presence of added catalyst. In both cases, the dissolved ozone concentration decreased over time because of natural decomposition and partial desorption back into the gas phase, with the decay being more rapid in the presence of the Fe-modified zeolite catalyst. The result indicates that the catalysts did not only promote pharmaceutical degradation but also enhanced the ozone decomposition, thereby increasing the formation of reactive oxygen species.

An oxidant control was performed in which the five-compound mixture (All-5) was sparged with pure oxygen without ozone. Under these conditions, no degradation was observed for SDZ, SFX, or CBZ. However, diclofenac showed a moderate decline in the two-hour ozonation treatment whereas ibuprofen presented a minor decrease (less than 10 %), as shown in Fig. 10. It should be noted that diclofenac is photo-labile: under simulated sunlight or UV irradiation, it has been shown to undergo significant direct photolysis [28], which may explain the ~60 % conversion observed in our oxygen-only run. However, in the actual ozonation experiments the reaction proceeded so rapidly—with complete conversion typically within 10 min—that any possible contribution from light-induced degradation is negligible in comparison to the dominant ozone-driven oxidation.

Overall, these results confirm that oxygen sparging and hydrodynamics alone cannot account for the substantial removal observed in the ozonation experiments. The control tests thus demonstrate that the pronounced degradation and mineralization trends in catalytic ozonation originate from ozone chemistry, further enhanced by heterogeneous catalysts.

To further confirm the precision of the analytical method and the stability of the experimental setup, selected ozonation experiments (non-catalytic IBU, catalytic IBUNa+CBZ mixture, and catalytic SFX single experiment) were repeated on different days under identical conditions; the resulting concentration–time profiles overlapped almost completely, demonstrating excellent reproducibility.

### 3.2.2. *Ozonation of single APIs*

The degradation behaviour of the studied APIs can be rationalized not only by their functional groups but also by their physicochemical properties. Table 3 summarizes key structural features, kinetic diameters, log $K_O$w values, and the expected ozone reactivity of each compound. The functional groups are key for determining the intrinsic chemical vulnerability of a molecule toward electrophilic ozone attack, while hydrophobicity (expressed as log $K_O$w) influences how readily a compound partitions between aqueous solution and catalyst surfaces.

Hydrophilic APIs (*low* log $K_O$w, i.e., sulfamethoxazole, sulfadiazine) remain mainly dissolved in water, where their reactivity depends strongly on functional group chemistry. By contrast, more hydrophobic APIs (*higher* log $K_O$w, i.e., diclofenac, ibuprofen) tend to associate with organic matter and catalyst surfaces, which can affect both their apparent degradation rates and the extent of mineralization achieved. Intermediate compounds such as carbamazepine illustrate how a balance between functional group reactivity (electron-rich double bond) and moderate hydrophobicity can favour both rapid ozone attack and catalytic enhancement. This comparison highlights that both molecular structure and hydrophobicity together steer the degradation kinetics. While functional groups dictate how reactive an API is toward ozone, hydrophobicity modulates its accessibility to catalytic sites and its environmental persistence.

After the ozonation of each API one by one, it was investigated how the chosen catalysts influenced their degradation kinetics. As can be seen in Fig. 11, these APIs differed in intrinsic reactivity in the ozonation experiments.

The comparison of rate constants for single-API ozonation with and without catalysts reveals clear differences in the reactivity that can be linked to molecular structure and size. In non-catalytic ozonation, carbamazepine (CBZ) and sulfamethoxazole (SFX) show the highest intrinsic rates, which is consistent with their electron-rich functional groups that are highly prone to ozone attack [11,14]. CBZ contains a reactive double bond in the dibenzazepine system that undergoes ozonolysis, while SFX features an isoxazole moiety enhancing the electron density and reactivity.

In contrast, diclofenac (DCF), ibuprofen (IBU), and sulfadiazine (SDZ) degraded more slowly due to less reactive functional groups. The aromatic ring in IBU, deactivated by carboxyl group (–COOH), is less susceptible to electrophilic ozone attack. DCF, with dichlorinated aromatic rings, is stabilized by electron-withdrawing chlorine substituents, which reduces the direct ozone reactivity and shift the degradation towards slower hydroxyl radical pathways. SDZ carries a sulfonamide (–$SO_2$NH–) and heteroaromatic pyrimidine, both resistant to electrophilic attack [14,31,32]

Introducing Fe-H-Beta and Fe-H-Y zeolite catalysts notably increased the ozonation rates for certain compounds. The CBZ degradation was roughly doubled ($k > 4.6\ min^{-1}$), probably because its small, planar structure (kinetic diameter ≈ 0.8 nm) facilitates diffusion into mesoporous channels where activated radicals are formed. More than twofold enhancement of degradation rate was observed for SFX, possibly due to its intermediate molecular size and the ability of the sulfonamide group (–$SO_2$NH–) to form hydrogen bonds or weakly coordinate with

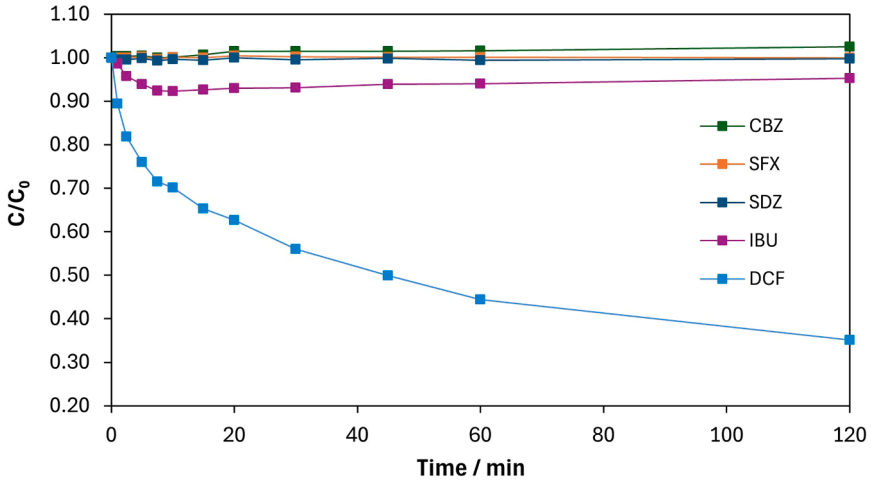


**Fig. 10.** Control experiment with 98 v-% oxygen flow (no ozone, 2 vol% $N_2$) in the five-component mixture.

**Table 3**
Structural features of studied APIs and their relation to ozonation reactivity.

| API | Key functional groups | Molecular size (nm)[a] | log $K_ow$ (hydrophob.) | Expected ozone reactivity | Notes |
|---|---|---|---|---|---|
| CBZ | Double bond in dibenzazepine, amide | 0.725 | 2.45 | Very high (ozonolysis-prone double bond) | Fastest degrading; fits into mesopores; strong catalyst enhancement. |
| SFX | Isoxazole, sulfonamide, aniline | 0.74 | 0.89 | High (electron-rich heteroaromatic) | Strongly enhanced by catalysts; isoxazole increases electron density. |
| DCF | Dichlorinated aniline + carboxylate | 0.82 | 4.51 | Moderate–low (Cl substituents deactivate rings) | Reacts mainly via •OH; sterically hindered in pores. |
| IBU | Aromatic ring + carboxylate (–COOH) | 0.84 | 3.97 | Low (electron-poor aromatic) | Limited catalyst enhancement; bulky side chain hinders access. |
| SDZ | Sulfonamide, pyrimidine | 0.69 | –0.09 | Low (heteroaromatic not very reactive to $O_3$) | Small enough for pores but lacks strongly reactive sites. |

[a] The reported molecular dimensions represent the largest distance between non-hydrogen atoms in the 3D structure, with a small correction added to account for atomic radii. These approximate overall sizes were estimated using the online molecular modelling tool MolView (https://molview.org/) and can be directly compared with the pore openings of the catalysts. Corresponding molecular structures are shown in Supplementary material Figure S9.

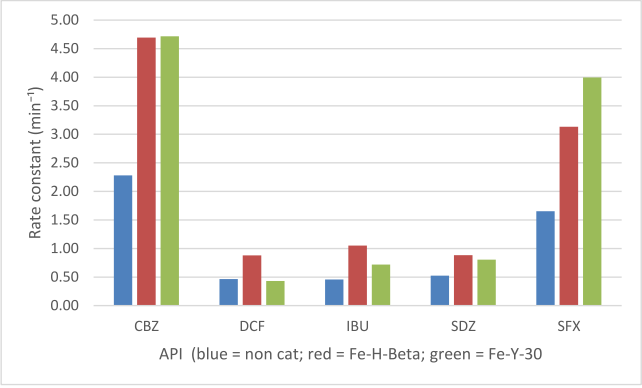


**Fig. 11.** The degradation rate constant for each API in the absence and in the presence of one catalysts: Fe-H-Beta or Fe-Y.

surface hydroxyl and metal sites. Similar surface–molecule interactions have been reported for metal-modified zeolites and mesoporous catalysts during catalytic ozonation [21,33].

By contrast, DCF and IBU show only modest improvements with catalysts. Their bulkier structures (dichlorophenyl in DCF, branched alkyl chain in IBU) likely hinders the diffusion into pores, restricting reactions to the external surface sites. SDZ, although a relatively small molecule, gains a little benefit due to its intrinsically low reactivity and weaker adsorption. Beltrán *et al* [34]. observed that under non-catalytic ozonation, DCF reacts mainly through a direct molecular ozone attack, whereas sulfonamides such as SFX follow a mixed mechanism involving both direct ozone reaction and hydroxyl-radical oxidation, underscoring that intrinsic molecular reactivity interacts with catalyst structure in determining degradation performance. Overall, the results underscore the dual role of the catalysts: enabling pore-based hydroxyl radical degradation for small, planar pharmaceuticals such as CBZ and SFX, while providing mainly surface-mediated reactivity for bulkier and less reactive compounds. This structure–activity relationship highlights the importance of tailoring pore size and morphology to optimize catalytic ozonation of pharmaceutical mixtures [15].

*3.2.2.1. Kinetic comparison with earlier research.* We have previously studied the catalytic ozonation of several of the chosen APIs used in the current work [6,17–19,21]. The substantially higher dissolved ozone concentration in the present setup (98 % $O_2$ feed, ~25 mg $L^{-1}$) is directly reflected in the IBU kinetics. When recalculated over the initial 0 – 30 min window, the earlier 90 % $O_2$ setup and 500 mL $min^{-1}$ gave $k_{IBU}$= 0.027 $min^{-1}$, whereas our optimized non-catalytic run yielded $k_{IBU}$= 1.164 $min^{-1}$ with same flow. This corresponds to a ca. 43-fold increase in the apparent rate, along with a fourfold increase in dissolved ozone concentration (from ~6 mg $L^{-1}$ to ca 30 mg $L^{-1}$-45 mg/L, depending on the flow velocity). Consequently, complete IBU degradation was achieved within minutes in the present work, compared to nearly an hour required under the earlier conditions. To ensure the efficiency of the ozonation system in the present setup, IBU ozonation was conducted under the previously applied conditions, i.e. 90 % $O_2$ / 10 % $N_2$ and 500 mL $min^{-1}$ flow rate, and very similar kinetics was obtained to those reported by Saeid *et al.* [21]. In addition, stepwise saturation experiments were carried out in pure water to estimate the relevant gas–liquid transfer parameters. From these experiments, the dissolved ozone concentration was found to approach ~45 mg $L^{-1}$ at 98 % $O_2$ feed, corresponding to a gas-phase ozone content of ~ 9–10 vol % when calculated from the Henry's law (H ≈ 0.01 M $atm^{-1}$). The approach was fitted with an exponential model giving a mass transfer coefficient of $k_La$ = 0.199 $min^{-1}$, which a is typical value to reach complete saturation in 20 min of ozonation. These values confirm that with the improved conditions, the solution is kept at its saturation level throughout kinetic experiments. The saturation curve is displayed in Fig. 8 whereas the data, equations and derivations are presented in Supplementary material S2.

### 3.2.3. Ozonation of binary and multi-component mixtures

To evaluate competitive effects under more realistic conditions, the degradation kinetics was investigated of both the binary and five-component API mixtures. Representative kinetic profiles for non-catalytic and catalytic ozonation are shown in Fig. 11 and Fig. 12, while a summary of the apparent pseudo-first-order rate constants is provided in Table 4. For completeness, the dataset including the calculated inhibition percentages is available in the Supplementary material (Tables S3a and S3b).

Rate constants were estimated by using a pseudo-first-order model, justified by the excess of ozone relative to the substrate. Because the reactions were extremely rapid, often complete within 5–10 min, only a limited amount of experimental data could be collected before the parent API was completely consumed. Nevertheless, the kinetic fits can be considered reliable and provide a rational basis for comparative analysis. While the pseudo-first-order approximation assumes an excess of oxidant, a molar balance at the start of the reaction shows that the total API concentration (0.816 mmol/L) actually exceeds the dissolved ozone (≈0.625 mmol/L at 30 mg/L), yielding an $O_3$/API molar ratio below unity (~0.77). This supports the idea that, particularly at the early stages, competition for ozone is chemically plausible and contributes to the observed inhibition.

*3.2.3.1. Non-catalytic ozonation.* In the absence of catalysts, most binary mixtures exhibited clear inhibition, consistent with competition for ozone, as illustrated in Fig. 12. This was most pronounced for CBZ – IBU mixture, where the rate constant of CBZ dropped by over 80 %

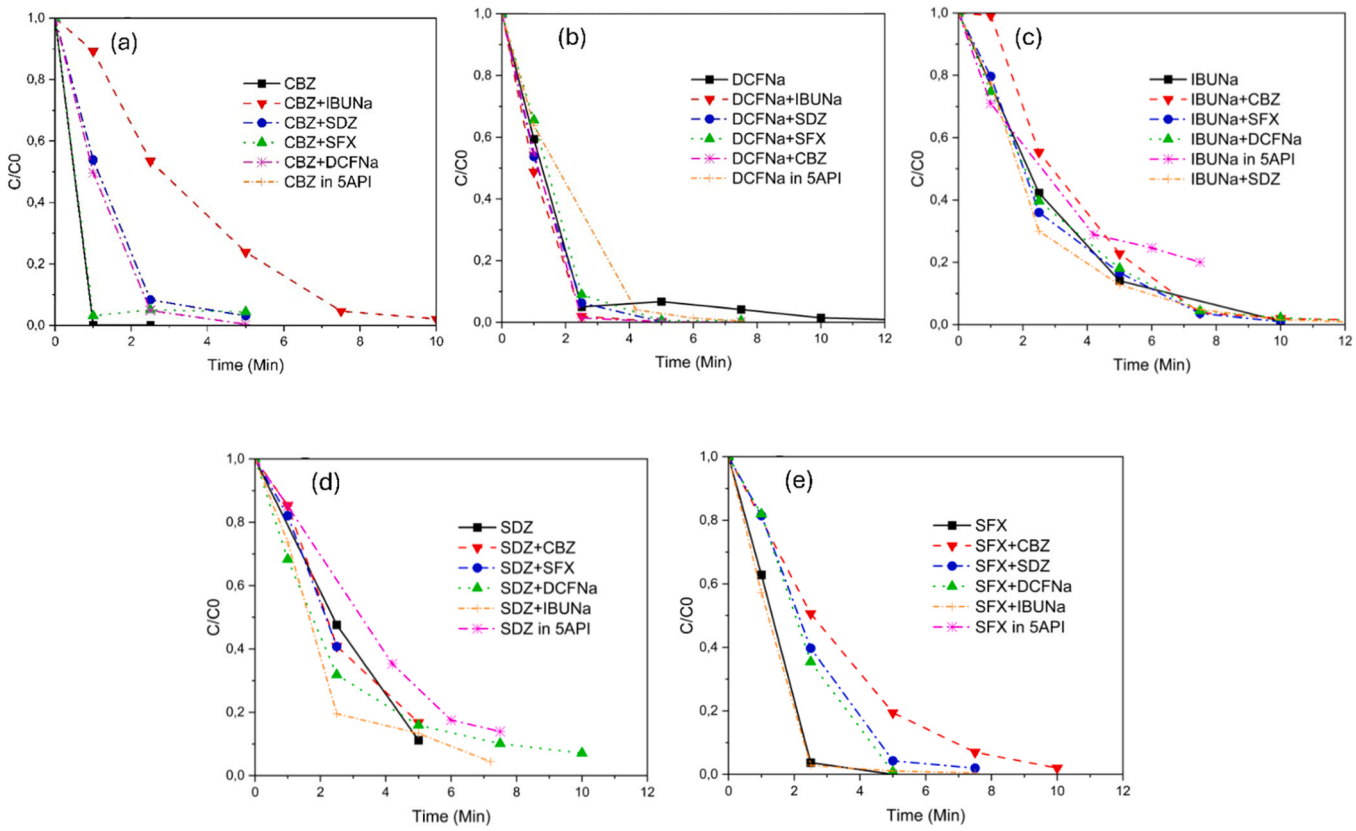


**Fig. 12.** Degradation profiles of the studied APIs in (a) CBZ, (b) DCF, (c) IBU, (d) SDZ, and (e) SFX, comparing single-API ozonation, binary mixtures, and the five-component mixture in the absence of catalysts. Conditions: gas flow rate: 250 mL $min^{-1}$ [APIs]= 40 mg/L, T = 20 °C, stirring rate = 1000 rpm.

**Table 4**
Single, and five-component mixture rate constants with or without catalyst.

| API | $k_{single,non-cat}$ ($min^{-1}$) | $k_{5-API,non-cat}$ ($min^{-1}$) | $k_{5-API,Beta}$ ($min^{-1}$) | $k_{5-API,Y}$ ($min^{-1}$) | Trend in binary / mixture |
|---|---|---|---|---|---|
| CBZ | 2.28 | 0.48 | 0.55 | 0.65 | Strongly suppressed, less in Y |
| DCF | 0.46 | 0.72 | 0.38 | 0.65 | Often promoted (non-cat), inhibited on Beta |
| IBU | 0.46 | 0.23 | 0.25 | 0.39 | Consistently suppressed |
| SDZ | 0.53 | 0.27 | 0.24 | 0.29 | Consistently suppressed |
| SFX | 1.65 | 0.17 | 0.16 | 0.37 | Strongly suppressed, partly relieved on Y |

compared to its single-API experiment. SDZ and IBU also suffered consistent inhibition with the other APIs present. In contrast, DCF often showed an enhanced degradation rate; when paired with IBU, its apparent rate more than doubled compared to single-API ozonation, indicating that interactions between the two compounds or differences in ozone reactivity influenced the overall kinetics [31].

SFX displayed intermediate inhibition characteristics, inhibited in some combinations, notably with CBZ, but less so in others. In the five-component mixtures, these trends became amplified: CBZ and IBU were severely inhibited, while DCF remained relatively more reactive, and SDZ appeared consistently suppressed, probably due to a weaker ozone affinity and competition with more electron-rich pharmaceuticals [35]. The competitive behaviour in the multi-component mixtures can be rationalized from the structural features in Table 3. Electron-rich aromatics such as CBZ and DCF react rapidly with ozone, while more polar APIs (SDZ and SFX) interact more strongly with acidic sites or rely more on radical pathways. These differences create distinct competition patterns, where some APIs consume ozone quickly and others preferentially occupy surface sites. This also explains why CBZ appears strongly inhibited, when compared to its very fast single-API rate, yet it still degrades rapidly within the mixture.

*3.2.3.2. Catalytic ozonation.* The role of catalysts in ozonation has been debated a long time [15,16]. While many studies report high efficiency, the underlying mechanisms remain only partly understood. Nawrocki and Kasprzyk-Hordem highlighted in a review article [15] several open questions: whether catalysts primarily promote the ozone decomposition into hydroxyl radicals or provide alternative surface-mediated pathways, how natural water constituents affect activity, and why some materials exhibit high performance while others do not. These uncertainties form the basis for interpreting our results, where introducing Fe-H-Beta altered several of the competitive trends observed under non-catalytic conditions. For some API pairs, inhibition was slightly alleviated, while for others it persisted or even intensified as shown in Fig. 13. For instance, the strong suppression of CBZ in the presence of IBU remained under catalytic conditions, with rates declining to zero, which is consistent with steric exclusion from the medium pores of Beta, and strong competition at the sites on the external surface. In contrast, DCF degraded more rapidly when present in mixtures than as a single component, suggesting that inter-compound or matrix effects enhanced its apparent reactivity under both catalytic and non-catalytic conditions. In the five-component mixture, the catalyst provided additional degradation routes but did not eliminate competitive effects: CBZ and IBU remained the most suppressed ones, while DCF and SFX retained a comparatively higher reactivity. The implications of these catalytic effects for the persistence and turnover of the transformation products are examined in the 3.2.4

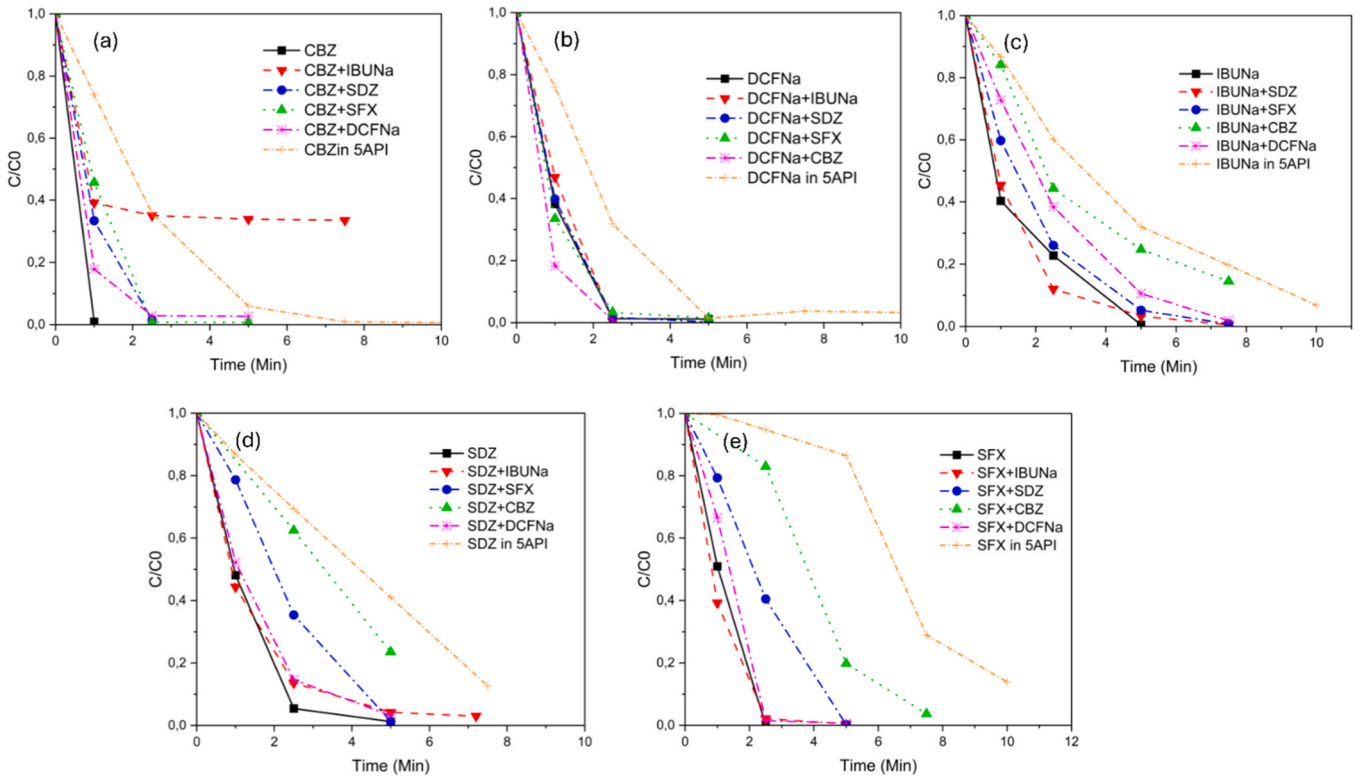


**Fig. 13.** Degradation profiles of the studied APIs in (a) CBZ, (b) DCF, (c) IBU, (d) SDZ, and (e) SFX, comparing single-API ozonation, binary mixtures, and the five-component mixture in the presence of 0.5 g Fe-H-Beta. Conditions: gas flow rate: 250 mL $min^{-1}$ , [APIs]= 40 mg/L, T = 20 °C, stirring speed= 1000 rpm.

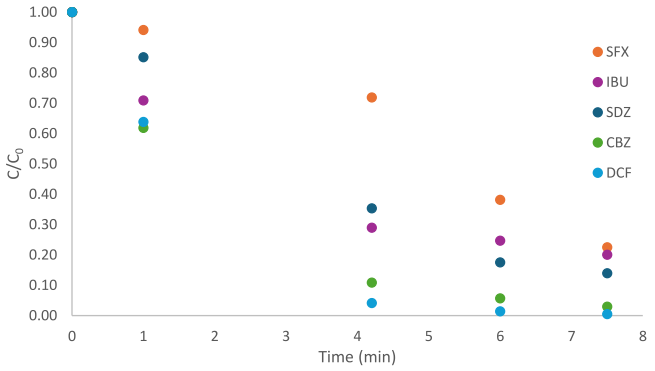


**Fig. 14.** Degradation of each API in the ozonation of the five-component mixture without any catalyst. Gas flow rate 250 mL $min^{-1}$ , T = 20°C.

*3.2.3.3. Comparison of the 5-component kinetics across non-cat and catalysts.* To reveal the mutual influence of reactants under realistic conditions, the simultaneous degradation of all five APIs was studied. Fig. 14 (non-catalytic), 15 (Fe-H-Beta), and 16 (Fe-H-Y) display the kinetic profiles. The corresponding apparent pseudo-first-order constants ($k$) are listed in Table 4 along with the binary data. The $k$ values were obtained from pseudo-first-order fits,

$$\ln\left(\frac{C}{C_0}\right) = -kt \quad (3)$$

using linear regression of ln(C/C₀) vs. time. The reactions were very fast, typically completed within 5–10 min, therefore only a few sample points could be taken before the concentration approached zero. Nevertheless, the fits were satisfactorily linear and provided reliable comparable constants under the experimental conditions. The compounds decayed rapidly, but inhibition patterns were pronounced. Using the pseudo-first order constants (Table 4), the order of apparent rates was

$$k_{DCF}(0.72) > k_{CBZ}(0.48) > k_{SDZ}(0.27) \approx k_{IBU}(0.23) > k_{SFX}(0.17)\ min^{-1}$$

Compared to single-API ozonation, SFX experienced the strongest inhibition (≈ −90 %), becoming the slowest in the mixture despite being fast when degraded alone (1.65 $min^{-1}$). Transformations of CBZ were strongly inhibited (≈ −79 %). DCF showed a net enhancement against its single-API experiment (≈ +54 %), in line with the binary experiments where DCF was promoted in the presence of certain compounds, notably IBU. IBU and SDZ showed moderate inhibitions (≈ −49 %). These results are consistent with the binary experiments: compounds that showed strong mutual inhibition in pairs (SFX, CBZ, SDZ) also exhibited the greatest suppression in the five-component system, whereas DCF again acted as a reaction promoter in the non-catalytic regime (Fig. 15).

*3.2.3.4. Fe-H-Beta-EIM zeolite catalyst.* With Fe-H-Beta, the overall

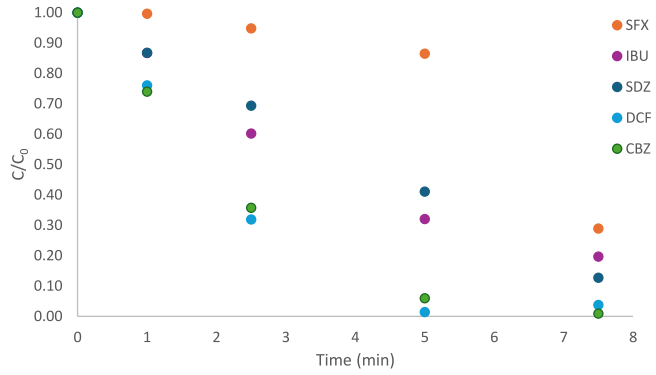


**Fig. 15.** Fe-H-Beta catalyzed ozonation of five-component mixture. Gas flow rate 250 mL $min^{-1}$ , T = 20°C.

removal progressed in similar rate to the non-catalytic experiment. The rate constants were:

$$k_{CBZ}(0.55) > k_{DCF}(0.38) > k_{IBU}(0.25) \approx k_{SDZ}(0.24) > k_{SFX}(0.16)\ \text{min}^{-1}$$

Again, SFX is the slowest and the most inhibited compound (≈ −95 % vs. its single-API catalytic rate of 3.13 $min^{-1}$). CBZ remains heavily inhibited (≈ −88 %), but not the slowest under Fe-H-Beta. Notably, DCF flips from enhancement in the non-catalytic five-component experiment to inhibition on Fe-H-Beta (≈ −57 % vs its single-API catalytic rate), indicating that the microporous, medium-pore framework alters the pathway: site competition and steric exclusion in Fe-H-Beta appear to suppress DCF's promoter-like behaviour observed in non-catalytic ozonation. IBU and SDZ are significantly inhibited on Beta (≈ −77 % and ≈ −73 %, respectively), which is consistent with their susceptibility to competition observed in the binary data.

*3.2.3.5. Fe-H-Y-EIM catalyst.* For Fe-H-Y, degradation of the five-compoment API mixture proceeded efficiently, with all the compounds removed within the first 7–8 min, as shown in Fig. 16. The apparent rate constants followed the order

$$k_{CBZ}(0.65) \approx k_{DCF}(0.65) > k_{SFX}(0.37) \approx k_{IBU}(0.39) > k_{SDZ}(0.29) \quad \text{min}^{-1}$$

Compared to single-API catalytic experiments, all compounds showed inhibition in the multicomponent system, but the extent was smaller than observed with Fe-H-Beta. CBZ, which was strongly suppressed under Fe-H-Beta (≈ −88 %), still degraded relatively rapidly on Fe-H-Y (≈ −77 % inhibition versus its single-API rate), remaining the fastest-degrading compound within the five-component mixture. This means that the inhibition is only relative to its very high single-API rate; within the mixture, CBZ is still among the fastest to degrade. DCF maintained a high rate constant, confirming its consistent reactivity in mixtures, although its promoter-like enhancement seen in the single-compound ozonation (3.2.2) was not observed with Fe-H-Y. SFX, the slowest degradation compound without a catalyst and with Fe-H-Beta, improved its reactivity compared to the other APIs under Fe-H-Y, reflecting the advantage of its wider super cages leading to less steric restrictions. IBU and SDZ remained among the more inhibited APIs, which is consistent with their weaker intrinsic ozone reactivity and competitive disadvantage.

Overall, Fe-H-Y provided a more balanced degradation profile than Fe-H-Beta, with less extreme suppression of individual APIs and higher uniformity across the mixture. The wider pore architecture of Y likely reduces the steric hindrance and allows simultaneous access of multiple APIs and intermediates to reactive sites, which helps to moderate competitive effects compared to the narrower-pore Beta framework.

It is unlikely that the observed inhibition in the five-component system originates from global ozone shortage, since ozone was supplied in large excess and pseudo-first-order kinetics was consistently observed. Instead, the data seem to point in the direction of competition

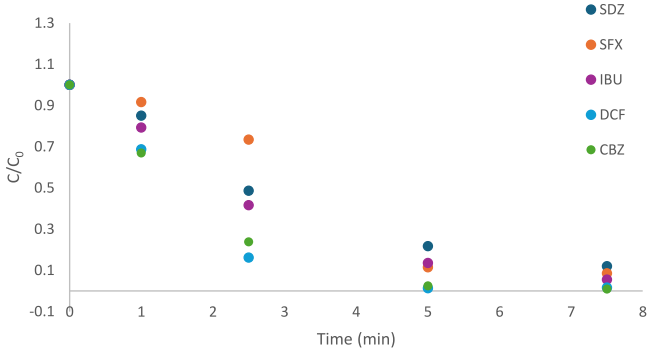


**Fig. 16.** Fe-H-Y catalysed ozonation of 5-component mixture. Gas flow rate 250 mL $min^{-1}$ , T = 20°C.

at the level of catalytic sites, steric exclusion from pores, and differences in the reactivity toward ozone-derived radicals.

The combined results of the binary and five-component experiments highlight three key points:

**(i)** Degradation behaviour in mixtures *cannot* be extrapolated directly from single-API tests, as *competitive and synergistic effects* strongly reshape the apparent kinetics.

**(ii)** Catalyst framework has a decisive influence, with Fe-H-Y alleviating steric constraints observed in Fe-H-Beta and providing a more balanced degradation profile.

**(iii)** Among the APIs, DCF emerges as the most resilient, often maintaining a higher relative reactivity than the other compounds, whereas the reaction rates of CBZ, IBU, SDZ, and particularly SFX are consistently the most suppressed ones, even though SFX benefits somewhat from the wider-pore architecture of Fe-H-Y.

These trends are summarized in Table 4, which compares the apparent pseudo-first-order (PFO) rate constants for single-API, binary, and five-component systems under both non-catalytic and catalytic ozonation. The summary highlights the pronounced inhibition of CBZ, IBU, SDZ, and SFX in mixtures, the relative resilience of DCF, and the moderating influence of Fe-H-Y compared with Fe-H-Beta.

The degradation of each pharmaceutical was treated as an apparent pseudo-first-order process with respect to solute concentration, since ozone was continuously supplied in large excess, maintaining a nearly constant oxidant level in the liquid phase. Under these excess-oxidant conditions, the reaction rate depends primarily on the pollutant concentration, and the apparent rate constant therefore integrates the combined effects of ozone transfer, intrinsic molecular reactivity, and catalyst interactions.

### 3.2.4. Kinetics of transformation products

Based on the catalytic effects described in 3.2.3, the kinetics of the transformation products (TPs) provide essential insight into the fate of APIs beyond their apparent disappearance in the bulk solution. Using LC–MS/MS data, the key descriptors were for each major TP were quantified, including the time of maximum abundance ($t_{max}$), normalized peak intensity ($A/A_0$), final remaining fraction, persistence index (final/peak), and half-decay time from the peak. Detailed TP metrics are compiled in Supplementary material (Table S4), while Table S5 summarizes comparisons with earlier single-API ozonation studies.

The LC–MS analysis confirmed the formation of characteristic transformation products previously reported for the individual APIs by Kråkström and Saeid et al [6,18–22]. Among these, the most persistent species—BQM/BQD (from CBZ), SDZ-P15 (from SDZ), and 4-hydroxy-DCF—were again detected under the mixed-API conditions (see Supplementary material Table S5). The occurrence of these diagnostic TPs demonstrates that the principal oxidation mechanisms—hydroxylation, ring rearrangement, and N-oxidation—remain dominant even when competitive reactions take place in the five-component mixture.

Next, we present the individual TP profiles and kinetic trends for each API, beginning with carbamazepine (CBZ) and its main transformation products BQM, BQD, and dihydro-CBZ.

*3.2.4.1. Carbamazepine (CBZ) TPs: BQM, BQD, and dihydro-CBZ.* CBZ is known to undergo a sequential CBZ → BQM → BQD pathway during the ozonation, with BQM (1-(2-benzaldehyde)-4-hydro-(1 H,3 H)-quinazoline-2-one) forming rapidly and subsequently oxidizing to BQD (1-(2-benzaldehyde)-(1 H,3 H)-quinazoline-2,4-dione) [18,21,36]. The transformation product data obtained by LC-MS reveals the following observations

i. BQM appears early, reaches a sharp maximum, and then decays as BQD accumulates.

ii. BQD is more persistent, with a higher persistence index and slower half-decay, confirming it as the dominant stable intermediate.
iii. Dihydro-CBZ was also detected at low concentrations, appearing already at t = 0 min in all runs (both non-catalytic as well as catalytic), which indicates it is a trace substance in the CBZ stock solution rather than TP formed by ozonation. Its rapid decline during reaction and intensity below 1 % of the CBZ peak area suggest that it is a short-lived side event rather than a recognized intermediate in the CBZ → BQM → BQD sequence.
iv. Under catalytic conditions, particularly Fe-H-Y, the BQM peaks were lower and decayed more rapidly, which is consistent with accelerated conversion to BQD or further oxidation.

Fig. 17 clearly shows the difference in reaction patterns between the three experiments without catalysts and those performed with catalysts.

*3.2.4.2. Ibuprofen (IBU) TPs.* The major observed TP was 1-oxo-IBU, which was formed rapidly but then decayed towards baseline, as displayed in Fig. 18. Its persistence index was moderate in the non-catalytic experiment but markedly decreased with Fe-H-Beta and Fe-H-Y catalysts, indicating a more rapid TP turnover in the presence of catalysts. The parent compound IBU was converted more rapidly using a catalyst, as can be seen in Fig. 18.

*3.2.4.3. Sulfadiazine (SDZ) TPs.* SDZ produced 2-aminopyrimidine (2-AP) as the dominant TP, according to Fig. 19. The small 2-AP peak emerged quickly and vanished very quickly as well. There was no clear enhancement by catalysis. The peak area of this particular TP was anyhow very small in comparison with the parental compound initial area (<0.01 %).

*3.2.4.4. Diclofenac (DCF) TPs.* The hydroxylated intermediate 4-OH-DCF dominated in the non-catalytic experiment, with peak areas up to ~250-fold (Beta) and ~900-fold (Y) higher than in the catalytic runs. Both Fe-zeolites strongly suppressed the accumulation of 4-OH-DCF, as illustrated in Fig. 20. Additionally, a trace ring-closed DCF product was detected in both absence and presence of catalysts, most likely corresponding to 8-chloro-9H-carbazole-1-acetic acid. This compound is known to occur as a minor impurity or secondary oxidation product of diclofenac, and its low abundance suggests that it has no significant influence on the overall degradation pathway.

Results are consistent with earlier reports of hydroxylated diclofenac derivatives as dominant ozonation products. Vogna *et al.* [31] showed that diclofenac reacts rapidly with ozone ($k \approx 1.8 \times 10^4$ $M^{-1}$ $s^{-1}$ at pH

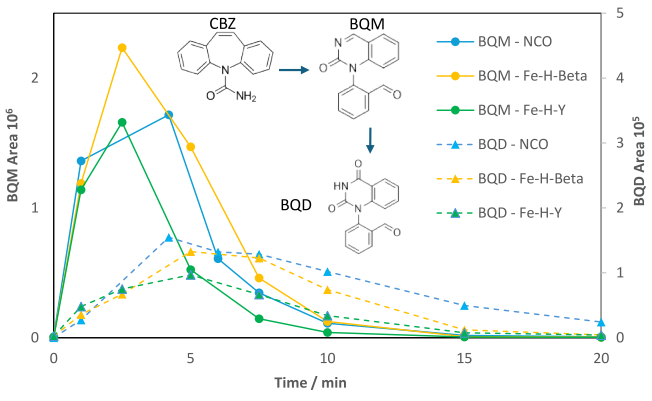


**Fig. 17.** Kinetics followed by LC-MS of CBZ transformation products under non-catalytic and catalytic ozonation. BQM (circles) peaks rapidly at ~15–20 % of the CBZ initial area and subsequently decays as BQD (squares) emerges. BQD remains at low levels (~1–2 %), and both catalysts further suppress its accumulation.

5–6) and yields mono-hydroxylated aromatic intermediates among its major transformation products. Our LC–MS results confirm this pathway, with 4-OH-DCF being the main non-catalytic product, also previously observed in single-compound studies by Saeid *et al.* [6]. Importantly, the strong suppression of 4-OH-DCF by Fe-zeolites in the multi-API system demonstrates that catalytic conditions can markedly decrease the persistence of this well-established intermediate.

*3.2.4.5. Sulfamethoxazole (SFX) TPs.* Although no SFX transformation products were detected in our mixture experiments, this is likely due to library limitations rather than the absence of degradation. Based on [30]established ozonation mechanisms and previous photochemical studies [30], it is highly probable that key transformation products such as hydroxylated SFX, sulfanilic acid–type fragments, and ring-cleaved amide derivatives were formed under our conditions. Representative structures of these expected products are provided in supplementary MOL files to support future identification.

*3.2.4.6. Mechanistic insights.* Semi-quantitative LC-MS area ratios ($TP_{max}$/Parent$_0$) highlight that CBZ's BQM is the dominant intermediate across all conditions (~15–20 %), whereas BQD remains low (~1–2 %) and is further suppressed by both catalysts, indicating accelerated conversion beyond BQD. Constantly, earlier $t_{max}$ values for Fe-zeolites (most pronounced for Fe-H-Y) indicate a faster sequential oxidation of BQM and BQD. For IBU, 1-oxo-IBU is clearly suppressed under catalytic conditions, showing lower maxima and an earlier decay, confirming faster TP turnover in the presence of Fe-zeolites. For SDZ, the signal of 2-aminopyrimidine was consistently very low in all experiments, preventing a clear distinction between the catalytic and non-catalytic effect. In sharp contrast, for DCF, the difference was striking: the 4-OH-DCF intermediate reached peak areas up to ~250-fold (Fe-H-Beta) or ~900-fold (Fe-H-Y) higher in the non-catalytic experiment compared with the catalytic cases, demonstrating that both of the studied Fe-zeolites strongly prevent the accumulation of this otherwise dominant intermediate. Dihydro-CBZ appears quickly at low abundance, consistently with a minor parallel route rather than a primary stage in the CBZ→BQM→BQD sequence. Collectively, the lower TP maxima and earlier formation reaction times in Fe-H-Y relative to Fe-H-Beta align with the FAU framework facilitating deeper, more rapid turnover of TPs.

*3.2.4.7. Comparison to our previous single-API studies.* The results obtained with the mixtures align with and extend prior single-API findings. For CBZ, the CBZ → BQM → BQD sequence was reproduced, but in the five-component mixtures, BQD stays low (~1–2 % of parent area) and is further decreased by Fe-zeolites, indicating faster turnover beyond BQD than typically seen in single-compound systems; Pt-/Pd-Y screening reported persistent BQM/BQD under non-catalytic ozonation. For IBU, the dominant 1-oxo-IBU forms rapidly and decays more quickly with Fe-Beta/Y, which is consistent with the work of Saeid and Kråkström and co-workers [6,17–19,21] where catalysts accelerated the IBU conversion and suppressed buildup of hydroxylated and ketone intermediates. For DCF, abundant hydroxylated TPs (e.g., 4-OH-DCF) are reported in single-API ozonation. In our mixture, Fe-zeolites suppress the 4-OH-DCF by ~250–900 × vs the non-catalytic case, pointing to a strong catalytic effect on TPs even under competitive conditions. For SDZ, Kråkström *et al.* [19] identified the persistent SDZ-P15 as a key bottleneck in single-API ozonation; in our mixtures mainly transient 2-aminopyrimidine was detected at a very low abundance (<0.01 %), suggesting that competitive adsorption and reactivity, and the Fe-zeolite surface are shifting the SDZ pathway away from SDZ-P15 within the time-window. For SFX, the literature reports multiple intermediates (*m/z* 98, 113, 158, 268, 298) formed via isoxazole-ring and S–N bond cleavage [32], but such compounds were not detected here. This is attributed to the absence of SFX TP molecular libraries in our LC–MS method rather than to their absence in the solution. It is therefore possible that some of these

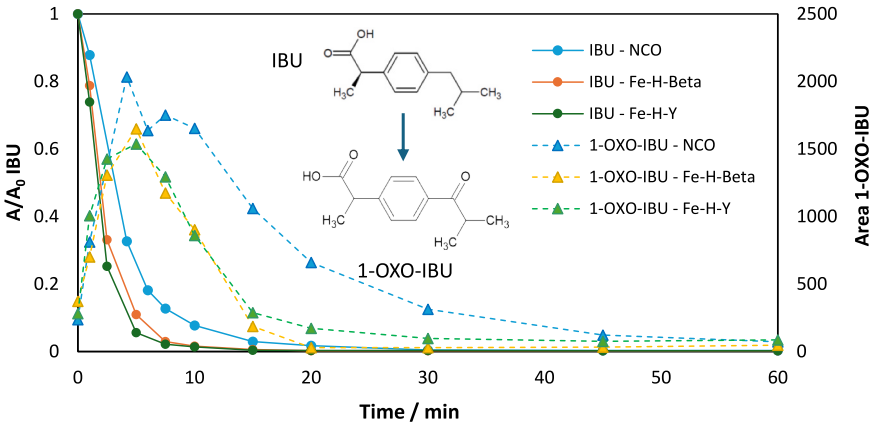


**Fig. 18.** LC-MS kinetics of IBU transformation. 1-oxo-IBU (triangles) forms rapidly and decays within minutes with catalysts whereas a prolonged reaction time is required without a catalyst.

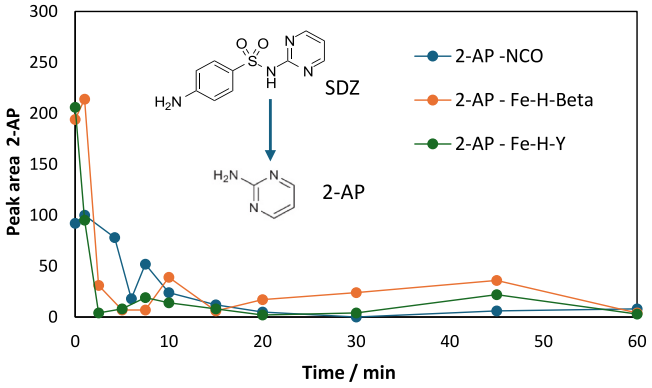


**Fig. 19.** Kinetics of SDZ TP 2-aminopyrimidine (2-AP) followed by LC-MS.

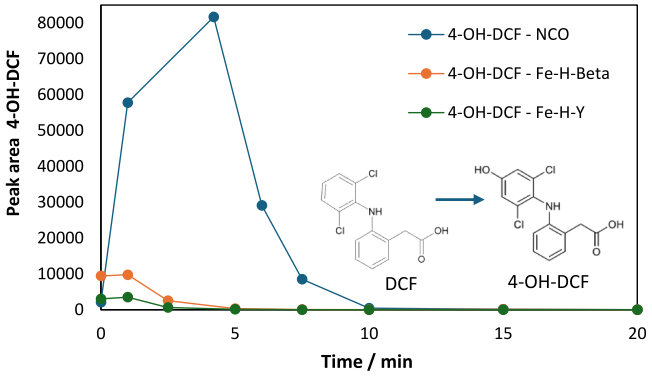


**Fig. 20.** LC-MS kinetics of DCF main TP4-OH-DFC transformations followed by LC-MS.

intermediates were transiently formed but rapidly oxidized downstream, leaving no persistent signals above baseline. Future targeted LC–MS analysis with expanded libraries will be required to confirm these pathways.

Across APIs, the mixture context and Fe-zeolite framework (especially Fe-H-Y) reduce the persistence of hallmark TPs reported in the single-API investigations, indicating accelerated TP turnover and pathway diversification under competitive, multi-component ozonation.

In summary, LC–MS analysis confirmed the formation of characteristic transformation products previously reported for the individual APIs ([6,18–22]). Among these, the most persistent species—BQM/BQD (CBZ), SDZ-P15 (SDZ), and 4′-hydroxy-DCF—were again detected under the mixed-API conditions (see Table S5). The appearance of these diagnostic TPs verifies that the primary oxidation pathways (hydroxylation, ring rearrangement, and N-oxidation) remain dominant even when competitive reactions occur in the five-component mixture.

### 3.3. Mineralization (TOC analysis)

The results with the five-component mixtures illustrate the challenge of treating realistic pharmaceutical effluents, where multiple compounds compete for ozone and hydroxyl radicals. Compared to single-compound experiments, the observed apparent rate constants were systematically lower for all APIs, underlining the strong inhibitory interactions in complex mixtures. This effect is particularly pronounced for ibuprofen and the sulfonamides, which are known to be less intrinsically reactive toward ozone due to electron-poor functional groups and steric hindrance.

The TOC data illustrated in Fig. 21 provide a clear demonstration that catalytic ozonation not only accelerates degradation of parent APIs but also enhances overall mineralization of organic carbon. In the absence of catalysts, 63 % of the TOC was removed, suggesting that the remaining part (37 %) is accumulated as partially oxidized intermediates and low molecular weight end products. With Fe-H-Y and Fe-H-Beta catalysts, however, the TOC conversion reached up to 82.2 % and 89.5 %, respectively, after 120 min of ozonation. This 30–40 % improvement indicates that the catalysts facilitate further oxidation of the intermediates and end products, likely by generating additional hydroxyl radicals within the pores or on the surface sites.

The higher performance of Fe-H-Beta compared to Fe-H-Y is consistent with its somewhat different pore architecture and higher micropore volume, which may promote diffusion and adsorption of smaller APIs and by-products, thereby enabling deeper oxidation. On

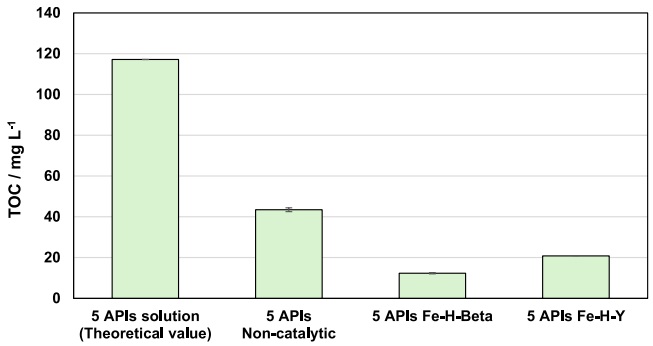


**Fig. 21.** TOC of initial vs non-catalytically ozonated as well as catalytically ozonated solution containing all five APIs.

the other hand, both catalysts clearly shift the balance from simple transformation of APIs toward more complete mineralization, which is a critical requirement for practical wastewater treatment applications.

In the literature, non-catalytic ozonation of pharmaceuticals and their mixtures typically results in partial mineralization, the TOC reduction on carbamazepine and diclofenac having similar limitations due to the accumulation of stable intermediates [11,14,34]. Against this benchmark, the present results clearly demonstrate the benefit of introducing Fe-zeolite catalysts. With Fe-H-Y, the TOC removal reached 82.2 %, and with Fe-H-Beta, as high as 89.5 % after 120 min, significantly exceeding the values commonly reported for non-catalytic systems. This performance highlights that the catalysts are not only accelerating the parent API degradation but also enable deeper oxidation of the intermediates toward mineralization. This kind of enhanced mineralization is of particular importance for practical water treatment, as it reduces the risk of persistent by-product accumulation and associated ecotoxicity.

### 3.4. Adsorption–desorption studies

#### 3.4.1. Introduction and methodological considerations

The kinetic experiments revealed a striking feature: while the kinetic ozonation experiments showed that the parent APIs disappeared rapidly ($t_{90}$% within minutes by HPLC), the transformation product (TP) peaks continued to grow for a prolonged period. This apparent paradox indicates that reactions proceed even in the absence of measurable bulk-phase APIs. A plausible explanation is that the parent molecules undergo fast adsorption into catalyst pores, followed by slower in-pore oxidation to smaller TPs, consistent with the adsorption–reaction coupling mechanism reported by Ikhlaq *et al.* [37]. To confirm this hypothesis, non-ozonated adsorption–desorption experiments were carried out for all five APIs on Fe-H-Beta and Fe-H-Y.

#### 3.4.2. Molecular accessibility and steric considerations

Before analysing the adsorption data, it is useful to compare the molecular size of the APIs with the pore dimensions of the catalysts. Table 5 summarizes the largest molecular dimensions of the studied compounds. Given the median pore widths of Fe-H-Beta (~0.67 nm) and Fe-H-Y (~0.76 nm), steric limitations are expected to play a major role, particularly in the narrower Beta framework. The smaller molecules, such as SDZ and SFX, are comparable in size to the pore openings and can access the microporous regions at least partially, whereas bulkier species such as DCF and IBU are largely restricted to pore mouths and external surfaces. This behaviour reflects their differing interactions with acidic sites: APIs with lower hydrophobicity (e.g., SDZ, SFX, based on log $K_o$w) can engage more readily with Brønsted acid sites inside the pores, whereas bulkier and more hydrophobic molecules are limited by steric constraints and thus interact mainly with external surface sites.

#### 3.4.3. Adsorption–desorption results

Figs. 22–23 and Table 6 present the time-dependent uptake and desorption behaviour for each API on the two catalysts. It should be noted that these experiments were performed with 100 mL solutions, compared to 1 L in the kinetic ozonation experiments. This corresponds to a significantly higher catalyst-to-substrate ratio, which likely enhances the apparent uptake capacity. Although direct numerical comparison with ozonation data is not straightforward, the higher ratio helps emphasize adsorption effects and clarifies mechanistic trends.

Adsorption kinetics of the pharmaceutical mixture was analyzed using the pseudo-first-order (PFO) model, which assumes that the rate of uptake is proportional to the number of available adsorption sites on the catalyst surface [38,39]. The model provides a good empirical description for diffusion-controlled processes where physisorption dominates and equilibrium is gradually approached as the number of free sites decreases. In this work, the PFO model reproduced the experimental adsorption–desorption profiles well for both catalysts, as shown in Figs. 22–23. The fitted parameters ($k_{ads}$, $k_{des}$, and $R^2$) are summarized in Table 6. The good agreement between experimental data and the PFO simulations suggests that the adsorption is mainly governed by film and intraparticle diffusion rather than chemical bonding. Slightly higher $k_{ads}$ values were obtained for Fe-H-Y, indicating faster surface uptake and better accessibility of its wider pore openings compared to Fe-H-Beta.

#### 3.4.3.1. The following metrics were extracted.

- Uptake after 90 min ($q_{90}$) and residual amount after desorption at 120 min ($q_{120}$)
- Desorption ratio:

$$desorption\ ratio(\%) = \frac{q_{120}}{q_{90}} \times 100 \tag{5}$$

- Hysteresis index:

$$Hysteresis\ index(\%) = 100 - desorption\ ratio \tag{6}$$

These indices capture the degree of irreversibility: a lower desorption ratio (higher hysteresis) indicates stronger retention and less reversible adsorption. Adsorption curves (0–90 min) were modelled using the pseudo-first-order (PFO) equation, which is one of the most widely applied kinetic formulations for describing liquid–solid adsorption systems [38,39]

$$(\mathrm{PFO}): \quad q_t = q_e(1 - e^{-k_1 t}) \tag{7}$$

where $q_t$ is the uptake at time $t$, $q_e$ the equilibrium capacity, and $k_1$ is the rate constant. Desorption (91–120 min) was modelled by PFO decay

$$(\mathrm{PFO}) \quad q_t = q_0 e^{-k_d(t-90)} \tag{8}$$

where $q_0$ is the retained amount at the start of desorption, and $k_d$ the desorption rate constant. The adsorption data were fitted using the pseudo-first-order (PFO) model, and the corresponding kinetic parameters — rate constants, equilibrium capacities, and desorption coefficients — are summarized in Table 6.

#### 3.4.4. Summary and interpretation of adsorption–desorption trends

For Fe-H-Beta, adsorption was moderate, with $q_{90}$ ranging from ~0.26 mg $g^{-1}$ (CBZ) to ~13.4 mg $g^{-1}$ (IBU). A significant fraction remained bound during desorption, especially for SDZ, CBZ, and DCF

**Table 5**
Comparison of the catalyst pore widths ($d_p$) and approximate kinetic diameters of APIs. Here, $d_p$ is the average (4 $V_t/S_{BET}$) metric and differs from crystallographic window sizes.

| Compound (API) | Approx. kinetic Diameter (nm) | Accessibility: Fe-H-Beta ($d_p$ =0.672 nm) | Accessibility: Fe-H-Y ($d_p$ =0.755 nm) |
|---|---|---|---|
| Sulfamethoxazole (SFX) | 0.74 | Borderline | Likely |
| Sulfadiazine (SDZ) | 0.69 | Borderline | Likely |
| Carbamazepine (CBZ) | 0.725 | Unlikely | Possibly |
| Ibuprofen (IBU) | 0.84 | Unlikely | Unlikely |
| Diclofenac (DCF) | 0.82 | Unlikely | Unlikely |

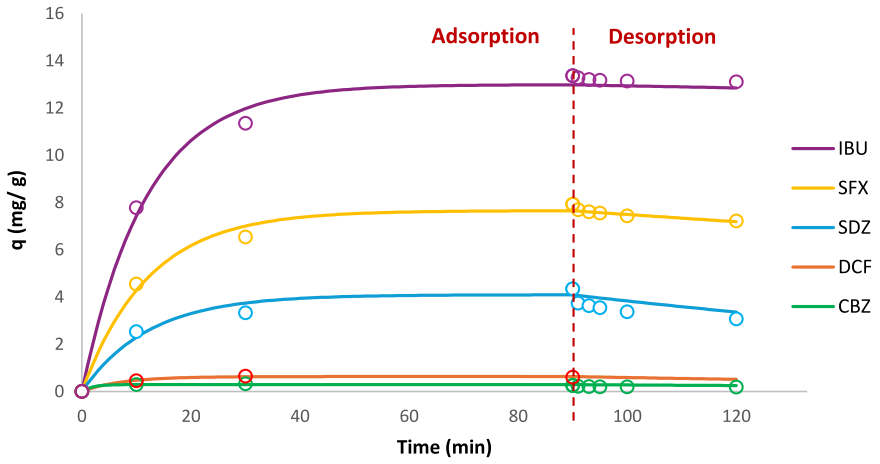


**Fig. 22.** Experimental and simulated adsorption–desorption profiles of a five-component API mixture on Fe-H-Beta. Circles represent experimental data points, and solid lines represent pseudo-first-order (PFO) model simulations using the fitted rate constants for both adsorption and desorption. The vertical dashed line marks the transition between the adsorption and desorption phases.

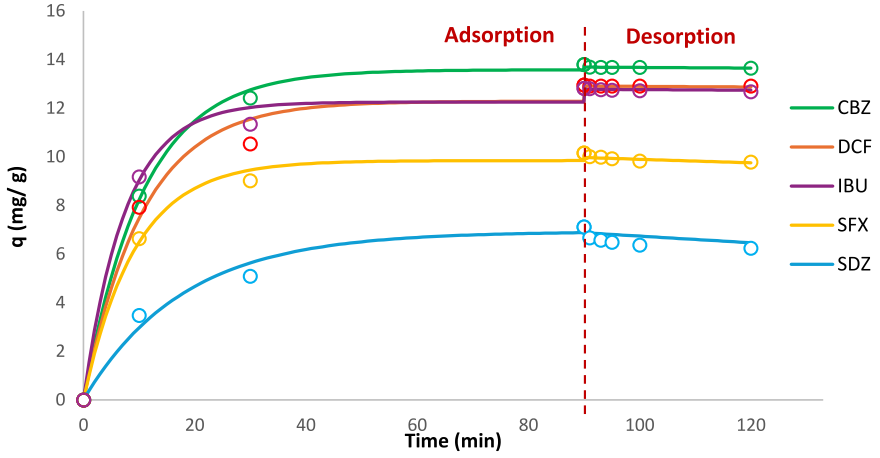


**Fig. 23.** Experimental and simulated adsorption–desorption profiles of a five-component API mixture on Fe-H-Y. Circles represent experimental data points, and solid lines represent pseudo-first-order (PFO) model simulations using the fitted rate constants for both adsorption and desorption. The vertical dashed line marks the transition between the adsorption and desorption phases.

**Table 6**
Adsorption–desorption metrics and kinetic parameters of APIs on Fe-H-Beta and Fe-H-Y.

| API | Cat. | $q_{90}$ (mg $g^{-1}$) | $q_{120}$ (mg $g^{-1}$) | Desorption ratio (%) | Hysteresis index (%) | $R^2$ (ads) | $k_{ads}$ | $k_{des}$ | $R^2$ (des) |
|---|---|---|---|---|---|---|---|---|---|
| SDZ | Beta | 4.34 | 3.07 | 70.7 | 29.3 | 0.99 | 0.082 | 0.0065 | 0.95 |
| SDZ | Y | 7.11 | 6.24 | 87.8 | 12.2 | 0.98 | 0.056 | 0.0026 | 0.91 |
| SFX | Beta | 7.9 | 7.2 | 91.0 | 9.0 | 1.00 | 0.082 | 0.0021 | 0.94 |
| SFX | Y | 10.2 | 9.8 | 96.3 | 3.7 | 0.99 | 0.11 | 0.0009 | 0.91 |
| CBZ | Beta | 0.3 | 0.2 | 71.7 | 28.3 | 0.96 | 0.57 | 0.0047 | 0.80 |
| CBZ | Y | 13.8 | 12.6 | 91.1 | 8.9 | 1.00 | 0.093 | 0.0001 | 0.90 |
| DCF | Beta | 0.6 | 0.4 | 72.1 | 27.9 | 0.99 | 0.138 | 0.0069 | 0.93 |
| DCF | Y | 12.9 | 11.4 | 88.1 | 11.9 | 1.00 | 0.094 | 0.0000 | — |
| IBU | Beta | 13.4 | 12.2 | 91.2 | 8.8 | 1.00 | 0.085 | 0.0003 | 0.64 |
| IBU | Y | 12.8 | 11.8 | 91.8 | 8.2 | 0.99 | 0.134 | 0.0005 | 0.85 |

$q_{90}$ = uptake at 90 min (end of adsorption phase); $q_{120}$ = retained amount after desorption (120 min); Desorption ratio = $q_{120}/q_{90} \times 100$; Hysteresis index = 100 – Desorption ratio; $k_{ads}$ = rate constant from adsorption model PFO; $k_{des}$ = desorption rate constant.

(hysteresis ~28–29 %), consistent with irreversible interactions and stronger fouling. This agrees with the pronounced losses of BET surface area and acidity observed after ozonation.

In case of *Fe-H-Y*, uptakes were generally higher (up to ~13–14 mg $g^{-1}$ for CBZ and DCF), while desorption was more complete. Hysteresis values were lower (3–12 %), indicating weaker binding and greater reversibility. The larger pore openings and higher micropore volume of Y allow molecules to move in and out more easily, preventing long-term pore blockage.

Table 6 condenses the comparative observations for each API, while Table 7 ranks them according to the desorption ratio/hysteresis. On Fe-H-Beta, the strongest retention was observed for SDZ, CBZ, and DCF, indicating a high fouling probability. On Fe-H-Y, SDZ and DCF showed the lowest reversibility, whereas SFX was the most easily desorbed,

**Table 7**
Qualitative interpretation of adsorption–desorption behaviour.

| Rank | API | Desorption ratio (%) | Hysteresis (%) | API | Desorption ratio (%) | Hysteresis (%) |
|---|---|---|---|---|---|---|
| | | Fe-H-Beta | | | Fe-H-Y | |
| 1 | SDZ | 70.7 | 29.3 | SDZ | 87.8 | 12.2 |
| 2 | CBZ | 71.7 | 28.3 | DCF | 88.1 | 11.9 |
| 3 | DCF | 72.1 | 27.9 | CBZ | 91.1 | 8.9 |
| 4 | SFX | 91.0 | 9.0 | IBU | 91.8 | 8.2 |
| 5 | IBU | 91.2 | 8.8 | SFX | 96.3 | 3.7 |

having lowest hysteresis.

These results help to resolve the kinetic paradox often reported in heterogeneous ozonation systems [16,37,40]: the rapid disappearance of APIs from the bulk phase reflects their fast adsorption into catalyst pores, while the delayed formation of transformation products arises from slower intra-pore oxidation and diffusion-limited release. Similar observations have been reported for zeolitic and alumina catalysts, where apparent degradation rates are largely governed by adsorption–reaction coupling rather than bulk-phase oxidation. Mechanistically, the catalyst performance and stability are controlled by steric matching between API size and pore aperture and adsorption reversibility. Fe-H-Beta, with narrower pores and stronger acid–API interactions, is more prone to irreversible adsorption and deactivation, while Fe-H-Y combines wider pores and higher desorption reversibility, maintaining textural integrity and long-term activity.

## 4. Conclusions

Catalytic ozonation of the five-API pharmaceutical mixture demonstrated substantial improvements in degradation and mineralization efficiency compared with non-catalytic ozonation. Optimization of the ozonation system, particularly the gas flow and mixing conditions, ensured stable ozone saturation in the liquid phase and resulted in several-fold faster kinetics compared with previous configurations. Both Fe-H-Y and Fe-H-Beta enhanced ozone utilization, with Fe-H-Y promoting faster conversion and Fe-H-Beta achieving higher total organic carbon (TOC) removal (82 % vs. 63 % in the non-catalytic system).

Adsorption–desorption studies showed that molecular size and polarity controlled the interactions between the APIs and the catalyst surface. Smaller and more polar compounds such as sulfadiazine and sulfamethoxazole exhibited stronger adsorption, whereas bulkier APIs (diclofenac, ibuprofen) were confined mainly to external surfaces. These behaviours correlated with the pore dimensions of the zeolites: Fe-H-Beta (0.67 nm) provided higher adsorption capacity but slower desorption than Fe-H-Y (0.75 nm).

Post-reaction analyses confirmed that Fe-H-Y retained a larger portion of its surface area and pore volume and showed much lower Fe leaching, indicating higher structural and chemical stability. TGA analyses revealed larger carbonaceous residues on Fe-H-Beta (≈23 mg $g^{-1}$ cat) than on Fe-H-Y (≈8 mg $g^{-1}$ cat), consistent with stronger by-product retention in its micropores. Acidity characterization supported these findings, showing that the stronger Brønsted acidity of Fe-H-Beta enhances adsorption but contributes to pore blocking during repeated operation. Fe-H-Y showed a small post-reaction increase in apparent acidity, most likely due to changes in surface accessibility rather than formation of new sites, aligning with its high structural stability.

Overall, the optimized ozonation conditions combined with catalyst selection significantly improved oxidation efficiency. Fe–H–Y emerged as the more durable and reusable catalyst, whereas Fe–H–Beta offered higher mineralization capacity during single-cycle treatments. The few short-chain carboxylic acids that were detected, represent expected intermediate oxidation products and are consistent with the high degree of mineralization observed in TOC analyses, rather than indicating incomplete degradation.

## CRediT authorship contribution statement

**Shey Jude Fale:** Writing – review & editing, Methodology, Investigation, Formal analysis, Data curation. **Soudabeh Saeid:** Writing – review & editing, Validation, Methodology, Conceptualization. **Matilda Kråkström:** Writing – review & editing, Supervision, Methodology, Data curation. **Dmitry Yu. Murzin :** Writing – review & editing, Validation, Supervision, Resources, Project administration, Conceptualization. **Ana Fernanda Núñez Núñez :** Writing – original draft, Visualization, Methodology, Investigation, Formal analysis, Data curation. **Tapio Salmi:** Writing – review & editing, Supervision, Resources, Project administration, Conceptualization. **Estéban Duverger:** Writing – original draft, Validation, Methodology, Investigation, Formal analysis, Data curation. **Nikke Saarinen:** Writing – review & editing, Validation, Methodology, Investigation, Formal analysis, Data curation. **Abdul Shahid:** Writing – original draft, Validation, Investigation, Formal analysis, Data curation. **Narendra Kumar:** Writing – review & editing, Validation, Supervision, Resources, Methodology, Data curation, Conceptualization. **Kari Eränen:** Supervision, Software, Resources, Project administration, Methodology, Conceptualization. **Patrik C. Eklund:** Writing – review & editing, Supervision, Resources, Project administration, Methodology, Formal analysis, Conceptualization. **Jyri-Pekka Mikkola:** Writing – review & editing, Visualization, Resources, Methodology, Funding acquisition, Conceptualization. **Pasi Tolvanen:** Writing – original draft, Supervision, Methodology, Investigation, Funding acquisition, Formal analysis, Data curation, Conceptualization.

## Declaration of Generative AI and AI-assisted technologies in the writing process

During the preparation of this work, the authors used ChatGPT (OpenAI, GPT-5 model) to assist with language refinement, consistency checking, and partial conceptual drafting of the graphical abstract. After using this tool, the authors critically reviewed, edited, and finalized all generated text and figures to ensure scientific accuracy and originality.

## Declaration of Competing Interest

The authors declare that they have no known competing financial interests or personal relationships that could have appeared to influence the work reported in this paper.

## Acknowledgements

Pasi Tolvanen gratefully acknowledges financial support from Liedon Säästöpankkisäätiö (personal research grant, 2024–2025, ref. 20240388) and from Svenska litteratursällskapet i Finland (SLS) (personal research grant, 2025–2026; supported by Ingrid, Margit och Henrik Höijers donationsfond II), whose contributions made this research possible. Pasi Tolvanen also thank Maa- ja vesitekniikan tuki Foundation for providing a travel grant that enabled participation in the International Conference on Environmental Catalysis (ICEC 2025), where part of this work was presented. Collaboration with the Erasmus Mundus Joint Master Programme IMATEC (International Master in

Technology and Management for Circular Economy) is appreciated for hosting the MSc thesis project of Ms Ana Fernanda Nuñez Nuñez and for providing financial support for analytical expenses through the student's scholarship. The participation of Estéban Duverger was made possible through the Erasmus+ internship exchange programme, which supported his three-month research placement during the summer 2025 (also supported by the French government program France2030 – EUR INTREE, reference ANR-18-EURE-0010). In Sweden the Bio4Energy program is acknowledged. The authors also thank the SpinChem AB for providing the SpinChem® equipment.

## Appendix A. Supporting information

Supplementary data associated with this article can be found in the online version at doi:10.1016/j.apcatb.2025.126274.

## Data availability

Research Link Provided

SEM images of Fe–H–Y and Fe–H–Beta zeolite catalysts (fresh and spent) used in catalytic ozonation of pharmaceutical mixtures (Zenodo)

## References

[1] T. aus der Beek, F.A. Weber, A. Bergmann, S. Hickmann, I. Ebert, A. Hein, A. Küster, Pharmaceuticals in the Environment—Global occurrences and perspectives, Environ. Toxicol. Chem. 35 (4) (2016) 823–835, https://doi.org/10.1002/etc.3339.

[2] S.R. Hughes, P. Kay, L.E. Brown, Global synthesis and critical evaluation of pharmaceutical data sets collected from river systems, Environ. Sci. Technol. 47 (2) (2013) 661–677, https://doi.org/10.1021/es3030148.

[3] D. Fatta-Kassinos, S. Meric, A. Nikolaou, Pharmaceutical residues in environmental waters and wastewater: current state of knowledge and future research, Anal. Bioanal. Chem. 399 (1) (2011) 251–275, https://doi.org/10.1007/s00216-010-4300-9.

[4] K. Kümmerer, The presence of pharmaceuticals in the environment due to human use—present knowledge and future challenges, J. Environ. Manag. 90 (8) (2009) 2354–2366, https://doi.org/10.1016/j.jenvman.2009.01.023.

[5] R.P. Schwarzenbach, B.I. Escher, K. Fenner, T.B. Hofstetter, C.A. Johnson, U. von Gunten, B. Wehrli, The challenge of micropollutants in aquatic systems, Science 313 (1979) (2006) 1072–1077, https://doi.org/10.1126/science.1127291.

[6] M. Kråkström, S. Saeid, P. Tolvanen, N. Kumar, T. Salmi, L. Kronberg, P. Eklund, Identification and quantification of transformation products formed during the ozonation of the non-steroidal anti-inflammatory pharmaceuticals Ibuprofen and Diclofenac, Ozone Sci. Eng. 44 (2) (2022) 157–171, https://doi.org/10.1080/01919512.2021.1898928.

[7] S. Brosché, Effects of Pharmaceuticals on Natural Microbial Communities: Tolerance Development, Mixture Toxicity and Synergistic Interactions, PhD thesis, University of Gothenburg, Sweden, 2010. Available at: https://gupea.ub.gu.se/handle/2077/23156.

[8] T. Heberer, Occurrence, fate, and removal of pharmaceutical residues in the aquatic environment: a review of recent research data, Toxicol. Lett. 131 (1–2) (2002) 5–17, https://doi.org/10.1016/S0378-4274(02)00041-3.

[9] T. Deblonde, C. Cossu-Leguille, P. Hartemann, Emerging pollutants in wastewater: a review of the literature, Int. J. Hyg. Environ. Health 214 (6) (2011) 442–448, https://doi.org/10.1016/j.ijheh.2011.08.002.

[10] U. von Gunten, Ozonation of drinking water: Part I. Oxidation kinetics and product formation, Water Res. 37 (7) (2003) 1443–1467, https://doi.org/10.1016/S0043-1354(02)00457-8.

[11] R. Rosal, A. Rodríguez, M.S. Gonzalo, E. García-Calvo, Catalytic ozonation of Naproxen and carbamazepine on titanium dioxide, Appl. Catal. B 84 (1–2) (2008) 48–57, https://doi.org/10.1016/j.apcatb.2008.03.003.

[12] European Commission, Directive (EU) 2024/3019 of the European Parliament and of the Council of 11 April 2024 on urban waste water treatment (recast), Official Journal of the European Union, L 202, 12.6.2024, p. 1–134. Available at: https://eur-lex.europa.eu/eli/dir/2024/3019/oj.

[13] K. Skalska-Tuomi, L. Kaijanen, J.M. Monteagudo, M. Mänttäri, Efficient removal of pharmaceuticals from wastewater: comparative study of three advanced oxidation processes, J. Environ. Manag. 375 (2025) 124276, https://doi.org/10.1016/j.jenvman.2025.124276.

[14] M.M. Huber, S. Canonica, G.-Y. Park, U. von Gunten, Oxidation of pharmaceuticals during ozonation and advanced oxidation processes, Environ. Sci. Technol. 37 (2003) 1016–1024, https://doi.org/10.1021/es025896h.

[15] J. Nawrocki, B. Kasprzyk-Hordern, The efficiency and mechanisms of catalytic ozonation, Appl. Catal. B 99 (1) (2010) 27–42, https://doi.org/10.1016/j.apcatb.2010.06.033.

[16] B. Kasprzyk-Hordern, M. Ziółek, J. Nawrocki, Catalytic ozonation and methods of enhancing molecular ozone reactions in water treatment. Applied Catalysis B: Environmental, Elsevier, December 15, 2003, pp. 639–669, https://doi.org/10.1016/S0926-3373(03)00326-6.

[17] S. Saeid, P. Tolvanen, N. Kumar, K. Eränen, J. Peltonen, M. Peurla, J. Mikkola, A. Franz, T. Salmi, Advanced oxidation process for the removal of ibuprofen from aqueous solution: a non-catalytic and catalytic ozonation study in a semi-batch reactor, Appl. Catal. B 230 (2018) 77–90, https://doi.org/10.1016/j.apcatb.2018.02.021.

[18] M. Kråkström, S. Saeid, P. Tolvanen, N. Kumar, T. Salmi, L. Kronberg, P. Eklund, Ozonation of carbamazepine and its main transformation products: product determination and reaction mechanisms, Environ. Sci. Pollut. Res. 27 (2020) 23258–23269, https://doi.org/10.1007/s11356-020-08795-0.

[19] M. Kråkström, S. Saeid, P. Tolvanen, T. Salmi, P. Eklund, L. Kronberg, Catalytic ozonation of the antibiotic sulfadiazine: reaction kinetics and transformation mechanisms, Chemosphere 247 (2020) 125853, https://doi.org/10.1016/j.chemosphere.2020.125853.

[20] S. Saeid, M. Kråkström, P. Tolvanen, N. Kumar, K. Eränen, M. Peurla, J.P. Mikkola, L. Maël, L. Kronberg, P. Eklund, T. Salmi, Synthesis and characterization of metal modified catalysts for decomposition of Ibuprofen from aqueous solutions, Catalysts 10 (7) (2020), https://doi.org/10.3390/catal10070786.

[21] S. Saeid, M. Kråkström, P. Tolvanen, N. Kumar, K. Eränen, J.-P. Mikkola, L. Kronberg, P. Eklund, M. Peurla, A. Aho, A. Shchukarev, T. Salmi, Advanced oxidation process for degradation of carbamazepine from aqueous solution: influence of metal modified microporous, mesoporous catalysts on the ozonation process, Catalysts 10 (2020) 90, https://doi.org/10.3390/catal10010090.

[22] S. Saeid, M. Kråkström, P. Tolvanen, N. Kumar, K. Eränen, J.P. Mikkola, L. Kronberg, P. Eklund, A. Aho, H. Palonen, M. Perula, A. Shchukarev, T. Salmi, Pt modified heterogeneous catalysts combined with ozonation for the removal of diclofenac from aqueous solutions and the fate of by-products, Catalysts 10 (3) (2020), https://doi.org/10.3390/catal10030322.

[23] M.C. Celander, Cocktail effects on biomarker responses in fish, Aquat. Toxicol. 105S (3) (2011) 72–77, https://doi.org/10.1016/j.aquatox.2011.06.002.

[24] W. Busch, S. Schmidt, R. Kühne, T. Schulze, M. Krauss, R. Altenburger, Micropollutants in European Rivers: a mode of action survey to support the development of effect-based tools for water monitoring, Environ. Toxicol. Chem. 35 (8) (2016) 1887–1899, https://doi.org/10.1002/etc.3460.

[25] C. Baerlocher, L.B. McCusker, D.H. Olson. Atlas of Zeolite Framework Types, 5th ed., Elsevier, Amsterdam, 2007, ISBN 978-0-444-53067-7.

[26] A.B. Spinchem, 2024, Rotating Bed Reactor (RBR): Applications and Products Brochure ⟨https://spinchem.com/media/v03nnhj5/spinchem-brochure-rbr-applications-and-products.pdf⟩(accessed 2025-10-28).

[27] D. Stradomska, D. Świętochowska, R. Kubica, U. Hanefeld, K. Szymańska, New type of basket stationary bed reactor for heterogeneous biocatalysis, Chem. Eng. Process. Process. Intensif. 194 (2023), https://doi.org/10.1016/j.cep.2023.109590.

[28] L.P. Li, Y.C. Jin, L. Fang, C. Zhang, Direct photolysis of diclofenac under simulated sunlight: transformation pathway and biological concerns, Chemosphere 307 (2022), https://doi.org/10.1016/j.chemosphere.2022.135775.

[29] I. St-Jean, M.M. Friciu, A. Monfort, J. MacMahon, J.M. Forest, S. Walker, G. Leclair, Stability of extemporaneously compounded suspensions of trimethoprim and sulfamethoxazole in amber plastic bottles and syringes, Can. J. Hosp. Pharm. 74 (4) (2021) 327–333, https://doi.org/10.4212/cjhp.v74i4.3194.

[30] S. Chandra, P. Jagdale, I. Medha, A.K. Tiwari, M. Bartoli, A.D. Nino, F. Olivito, Biochar-supported TiO2-based nanocomposites for the photocatalytic degradation of sulfamethoxazole in water—a review, Toxics 9 (11) (2021) 313, https://doi.org/10.3390/toxics9110313.

[31] D. Vogna, R. Marotta, A. Napolitano, R. Andreozzi, M. d'Ischia, Advanced oxidation of the pharmaceutical drug diclofenac with UV/H2O2 and ozone, Water Res. 38 (2) (2004) 414–422, https://doi.org/10.1016/j.watres.2003.09.028.

[32] M.M. Gómez-Ramos, M. Mezcua, A. Agüera, A.R. Fernández-Alba, S. Gonzalo, A. Rodríguez, R. Rosal, Chemical and toxicological evolution of the antibiotic sulfamethoxazole under ozone treatment in water solution, J. Hazard Mater. 192 (1) (2011) 18–25, https://doi.org/10.1016/j.jhazmat.2011.04.072.

[33] H. Chen, J. Wang, Catalytic ozonation of sulfamethoxazole over Fe3O4/Co3O4 composites, Chemosphere 234 (2019) 14–24, https://doi.org/10.1016/j.chemosphere.2019.06.014.

[34] F.J. Beltrán, A. Aguinaco, J.F. García-Araya, Application of ozone involving advanced oxidation processes to remove some pharmaceutical compounds from urban wastewaters, Ozone Sci. Eng. 34 (1) (2012) 3–15, https://doi.org/10.1080/01919512.2012.640154.

[35] M.M. Gómez-Ramos, A. Pérez-Parada, J.F. García-Reyes, A.R. Fernández-Alba, A. Agüera, Use of an accurate-mass database for the systematic identification of transformation products of organic contaminants in wastewater effluents,

J. Chromatogr. A 1218 (44) (2011) 8002–8012, https://doi.org/10.1016/j.chroma.2011.09.003.
[36] T. Kosjek, H.R. Andersen, B. Kompare, A. Ledin, E. Heath, Fate of carbamazepine during water treatment, Environ. Sci. Technol. 43 (16) (2009) 6256–6261, https://doi.org/10.1021/es900070h.
[37] A. Ikhlaq, D.R. Brown, B. Kasprzyk-Hordern, Mechanisms of catalytic ozonation on alumina and zeolites in water: formation of hydroxyl radicals, Appl. Catal. B 123–124 (2012) 94–106, https://doi.org/10.1016/j.apcatb.2012.04.015.
[38] Y.S. Ho, G. McKay, Pseudo-second order model for sorption processes, Process Biochem 34 (1999) 451–465, https://doi.org/10.1016/S0032-9592(98)00112-5.
[39] E.D. Revellame, D.L. Fortela, W. Sharp, R. Hernandez, M.E. Zappi, Adsorption kinetic modeling using pseudo-first order and pseudo-second order rate laws: a review. Cleaner Engineering and Technology, Elsevier Ltd, December 1, 2020, https://doi.org/10.1016/j.clet.2020.100032.
[40] J. Wang, Z. Bai, Fe-based catalysts for heterogeneous catalytic ozonation of emerging contaminants in water and wastewater. Chemical Engineering Journal, Elsevier B.V, 2017, pp. 79–98, https://doi.org/10.1016/j.cej.2016.11.118.